ACOUSTIC CHARACTERIZATION OF SUDAN BLACK NANOBUBBLES FOR MULTIMODAL ULTRASOUND & PHOTOACOUSTIC IMAGING

By

Dana Wegierak

Bachelor of Science, Medical Physics

Ryerson University, 2020

A thesis presented to Ryerson University

in partial fulfillment of the requirements

for the degree of

Master of Science

in the program of

Biomedical Physics

Toronto, Ontario, Canada, 2020

Declaration of Authorship

I, Dana Wegierak, hereby declare that I am the sole author of this thesis. This is a true copy of the thesis, including any required final revisions, as accepted by my examiners.

I authorize Ryerson University to lend this thesis to other institutions or individuals for the purpose of scholarly research.

I further authorize Ryerson University to reproduce this thesis by photocopying or by other means, in total or in part, at the request of other institutions or individuals for the purpose of scholarly research.

I understand that my thesis may be made electronically available to the public.

"Nobody ever figures out what life is all about, and it doesn't matter. Explore the world. Nearly everything is really interesting if you go into it deeply enough."

Richard Feynman

ACOUSTIC CHARACTERIZATION OF SUDAN BLACK NANOBUBBLES FOR MULTIMODAL ULTRASOUND & PHOTOACOUSTIC IMAGING

Master of Science, Biomedical Physics

Dana Wegierak

Ryerson University, 2020

Abstract

Dyed, shelled, nanobubbles (NBs) have recently been proposed as contrast agents for multimodal ultrasound-photoacoustic (US-PA) imaging. However, changes to the shell composition due to the presence of the dye can modify the response of bubbles to ultrasound. In this work, the effects of the dye, Sudan Black B, on a formulation of lipid shelled NBs are studied. Formulations were produced with increasing concentration of Sudan Black B. The size and concentration of activated NBs were tested. The surface tension of bulk lipid solution was measured using pendant drop tensiometry and activated bubble solutions were measured for single bubble and bubble population response to incident ultrasound. While results show no statistically significant effect of Sudan Black concentration on bubble concentration or size, surface tension increased linearly with dye concentration to a maximum increase of 13%. With the addition of Sudan Black B, single bubble experiments show an increase in the contribution of bubble growth signals, a decrease in contribution of nonlinear signals, and a decrease in bubble destruction. The results presented in this work indicate that the presence of Sudan Black B in the lipid shell of a nanobubble may increase the shell permeability impacting stability of the bubble population and their potential for multimodal US-PA imaging.

Acknowledgements

First and foremost, I would like to thank my supervisor Dr. Michael Kolios. Dr. Kolios has been a relentless source of support through the duration of my work in his lab. Dr Kolios, I am so grateful for your support and guidance. Thank you for your passion; you taught me that one never need be uninterested in a study, only disinterested. I also extend my thanks to my committee members, Dr. Karshafian, and Dr. Kumaradas for their input and feedback.

To all members of the Kolios lab, I am sincerely thankful. For the contributions of Grace Fishbein, Charlotte Ferworn, and Elizabeth Berndl, thank you so much. Also for their advice, scientific discussion and friendship I have to thank Grace Fishbein, Morgan Maher, Charlotte Ferworn and Elizabeth Berndl. Your friendships are invaluable. I'm so grateful to have had the opportunity to get to know you all and to learn and grow together.

To Dr. Exner and her lab, without whom this work would not be possible, my thanks are numerous. Dr. Exner, thank you for encouraging me and being my mentor. Your belief in me has meant so much. To the Exner lab, you all have inspired me. Thank you for your being so welcoming and collaborative. For the contributions of Al de Leon, Eric Abenojar, and Jinle Zhu, thank you so much.

To the SciXchange team, I am forever grateful. Your passion in science communication has helped me stay true to my beliefs and principles. You have empowered me to share what I love with others. Thank you all, so much.

To my family that has never stopped encouraging me or focussing me, thank you. To my parents, thank you for your love and care. To my siblings, thank you for keeping me tough as nails.

To Andrei, thank you for being here for me. Thank you for supporting me and encouraging me, even when I was ready to give up. Thank you for being my team-mate. I don't do anything without you.

To all of my friends, family and co-workers, thank you for pushing me to be better.

Contents

List of Tables

List of Figures

List of Abbreviations

ANOVA	**An**alysis **O**f **Va**riance **s**ound
arPA	**a**coustic **r**esolution **PA**
DBPC	1,2-dibehenoyl-sn-glycero-3-phosphocholine
DDI	**D**egassed and **Dei**onized
DPPC	1,2-dipalmitoyl-sn-glycero-3-phosphate
DPPE	1,2-dipalmitoyl-sn-glycero-3-phosphoethanolamine
FDA	**F**ood and **D**rug **A**dministration
G	**G**lycerol
ICG	**I**ndo**C**yanine **Green**
MB	**M**icro**b**ubble
mPEG-DSPE	1,2-distearoyl-sn-glycero-3-phosphoethanolamine-N -[methoxy(poly(ethylene glycol))-2000]
NB	**N**ano**b**ubble
p_1	**p**eriod **1** oscillation
$p1_{diss}$	**p**eriod **1** dissolution oscillation
$p1_{growth}$	**p**eriod **1** growth oscillation
p_n	**p**eriodic **n**onlinear oscillation
PA	**P**hoto**a**coustic
PAnDs	**P**hoto**a**coustic **nanoDroplets**
PBS	**P**hosphate **B**uffered **S**aline
PDI	**P**erylene**Di**mide
PFC	**Per**fluouro**c**arbon
PG	**P**ropylene **G**lycol
ROI	**R**egion **O**f **I**nterest
RMM	**R**esonant **M**ass **M**easurement
SNR	**S**ignal to **N**oise **R**atio
SB	**S**udan **B**lack
SB	**S**udan **B**lack **N**ano**b**ubbles
TEM	**T**ransmission **E**lectron **M**icroscopy
UCA	**U**ltrasound **C**ontrast **A**gent
US	**U**ltra**s**ound

List of Symbols

μ_a	absorption coefficient
g	anisotropy factor
ρ	density
ρ_e	equilibrium pressure
ϕ	fluence
Γ	Grüneisen parameter
Z	impedance
κ_i	isothermal compressibility
κ	polytropic exponent
p_o	pressure
r	radius
rf	reflection fraction
f_0	resonance frequency
μ_s	scattering coefficient
v_s	speed of sound
C_P	specific heat capacity at constant pressure
C_V	specific heat capacity at constant volume
A_e	specific optical absorption
τ_s	stress relaxation time
η_{th}	thermal conversion efficiency
β	thermal expansivity
τ_{th}	thermal relaxation time

Chapter 1

Introduction

The morphology of the microvasculature can be used as a marker for disease detection because it is altered in many diseases, including cancer [1]. For this reason, medical imaging modalities that can effectively assess the morphology of microvasculature are important. In photoacoustic (PA) imaging, absorption of laser irradiation by components in tissue such as cells causes a thermoelastic expansion which generates ultrasound waves detected as PA signal. Hemoglobin from red blood cells is a strong light absorber and therefore generates high amplitude PA signal relative to other endogenous chromophores [1]. This can provide functional information of the microvasculature. In ultrasound (US) imaging, acoustic waves are generated by a transducer, transmitted through tissue, and reflected off of boundaries that exhibit differences in acoustic impedance. This has been used in robust morphological investigations of microvasculature. Morphological and functional information from US and PA imaging respectively has the ability to evaluate tumour morphology while tracking tumour metabolism [2] as a result of the microvascular imaging abilities. As such, US-PA multimodal imaging is a promising tool for early tumour detection and diagnosis.

Despite the potential of US-PA multimodal imaging, there are cases in which both modalities fall short. Relatively small differences in acoustic impedance limit ultrasound contrast [3]. Additionally, the number of photons available for initiating the PA effect significantly decreases with depth, which results in lower amplitude acoustic waves that may not be sensed by the transducer [3]. There is a critical need to: (1) extend the imaging depth of PA imaging and (2) enhance US contrast, to improve diagnostic imaging of malignant disease. One way to address this problem is to develop contrast agents for multimodal US-PA imaging.

1.1 Ultrasound Imaging and Acoustic Interactions

Ultrasound (US) imaging relies on the propagation of mechanical pressure waves (acoustic waves with frequency > 20 kHz) through a medium. In biomedical US imaging, inhomogeneous density of tissue causes mechanical property fluctuations from which a portion of the sound wave is reflected back toward the source [4]. The depth x of the scattering structure is determined through:

$$x = \frac{vt}{2} \tag{1.1}$$

where v is the speed of sound in the medium (0.154 [cm/μs] in water) and t is the time for the sound wave to be delivered from the wave source to the point of reflection and further to the point of detection. In clinical US imaging applications the source and the detector are usually the same transducer.

Acoustic scattering describes the reflection of an acoustic wave from an object the size of the wavelength or smaller. Red blood cells, for example, act as

Rayleigh scatterers because they are much smaller than incident acoustic waves for typical transducers. A 5 MHz acoustic wave has wavelength of 300μm in comparison to a red blood cell with a radius of approximately 8μm. Increasing the incident frequency increases the scattering from smaller objects. The best spatial detail in US is obtained when imaging at higher frequencies [4][5]. For example, as US frequency is increased to 50 MHz, an axial resolution and lateral resolution of better than 20 and 100 microns respectively for an f-number tranducer of 2.9 can be achieved [6]. Frequency dependent scattering interactions, however, contribute to frequency dependent US attenuation. US attenuation is higher for higher frequencies. The maximum propagation length of a typical US wave averages at approximately 300 wavelengths, directly limiting penetration depth in US imaging [4]. The relationship of frequency dependent attenuation is approximately linear for soft tissue. At 50 MHz, used in high-frequency US imaging, a depth of penetration of approximately 8-9 mm could be expected in most tissue types [6]. Most clinical US imaging systems employ frequencies in the range of 2 MHz to approximately 15 MHz.

US contrast is a consequence of differences in acoustic impedance which causes distortions of incoming acoustic waves. However, differences in acoustic impedance among tissue types, especially soft tissue, are often too small and cause situationally limited contrast in US images [2]. In the human body, the acoustic impedance of tissue spans a narrow range of 1.33-1.74 $\times 10^6$ [kg/m^2 s] with the exception of the lungs at 0.26 $\times 10^6$ [kg/m^2 s] and bone tissue spanning from 3.75-7.38 $\times 10^6$ [kg/m^2 s]. Ultrasound contrast agents are used to enhance the differences of acoustic impedance at locations of soft tissue boundaries, particularly for highly vascularized systems where blood exhibits an acoustic impedance of 1.65 $\times 10^6$ [kg/m^2 s].

1.1.1 Ultrasound Contrast Agents

The amount of reflection that occurs in a perpendicular direction from a tissue boundary is expressed by the reflection coefficient or reflection fraction (rf).

$$rf = \frac{(Z_2 - Z_1)^2}{(Z_2 + Z_1)} \tag{1.2}$$

Z_1 and Z_2 represent the impedance in two neighbouring materials at their boundary (ie. at the boundary of the blood pool ,Z_1, and it's vessel wall, Z_2). A successful contrast agent for US, therefore, must have either high or low acoustic impedance in comparison to neighbouring soft tissue. The reflection fraction for gas (0.0004×10^6 [kg/m^2 s]) compared to bone (7.38×10^6 [kg/m^2 s]) and water (1.48×10^6 [kg/m^2 s]) can be used to narrow the search for an ideal agent. Upon calculation, one finds that the rf for air:water is roughly 2x higher than for bone:water ($rf_{air} = 99.95\%; rf_{bone} = 44.34\%$). As a result, US contrast agents typically employ a gas vesicle to achieve an increase in acoustic impedance mismatch with surrounding tissue.

The first reported use of contrast agents, by Gramiak and Shah (1968), led to the conclusion that increased reflectivity was caused by microbubbles of gas [7]. Microbubbles (MBs) are now the dominant agent used for US enhancement. MBs are gas bubbles less than 10 μm and on average 2-3 μm in diameter. They are often stabilized with a protein, polymer or lipid shell [8][9][10]. In clinical use, MBs are injected intravenously to enhance ultrasound image contrast. Significant work has been done over the years investigating the mechanism of US contrast by MBs. However, the success of MBs is highly attributed to their dynamical response to an

incident US wave. Ongoing attention is offered to the optimization of MB dynamics under acoustic stimulation.

Bubble Dynamics

As US waves encounter a MB, the MB is subject to the compression and rarefaction of the pressure wave. In a simple, low pressure case (<50kPa) the bubble behaves linearly and it's oscillations are spherically symmetric during the acoustic interaction [11]. The compression component of the acoustic wave causes the MB to shrink in size as the gas core is compressed [12]. Likewise, in the rarefaction phase of the wave, the MB expands and the radius increases. As such, in a linear response of a MB to US, a bubble oscillation will have a consistent minimum and maximum shell radius throughout the US excitation [13]. Under such conditions the amplitude of oscillation of the bubble would be proportional to the amplitude of the incident US wave. A backscatter wave proportional in intensity to the incident wave would be generated.

For moderate acoustic pressures (50 to 200 kPa), nonlinear oscillations occur, giving rise to harmonics and subharmonics [11]. As the pressure amplitude of the US wave increases a bubble can expand with the sound field but cannot contract equally. This is because the volume of entrapped gas reaches a limit to which it can be compressed. A consequence of the asymmetry between the compression and expansion of the bubble is that the oscillations of MBs in an acoustic field can behave nonlinearly [8][12][14]. The nonlinear behaviour of MBs is a widely investigated area of interest [15][16][17] and has been thought to be the main driver for effective contrast enhancement.

Knowledge of the oscillatory behavior of the bubble including harmonics is necessary to optimize bubble applications [18]. Nonlinear response can also occur through bubble resonance. Resonance occurs when an external force is applied to a system at a rate that is equal to the natural frequency of the system. A bubble will demonstrate prolonged increased amplitude of oscillation when sonicated at its resonance frequency. The resonance frequency of an un-encapsulated MB with 2μm diameter is 3.8 MHz [11]. Like other resonant systems, harmonic energy can be detected in the backscattered ultrasound signal such as energy at the subharmonic, ultraharmonic, and higher harmonic frequencies. It has been shown that the bubble oscillator can exhibit $(1/2), (1/3), (1/4), (1/5)$, or higher order subharmonics as well as period doubling ($2f_0$), ultraharmonics ($nf_0/2$ where $n > 1$), superharmonics (f_0), and chaos. Harmonic nonlinear signals can be filtered using imaging pulse sequences with a modulated phase, frequency and amplitude to separate the MB signal from background tissue signal, further enhancing image contrast [12].

It has been shown that, as the acoustic pressure amplitude is increased, the resonance frequency of a lipid-shelled microbubble tends to decrease in comparison with its linear resonance frequency [19][18]. In general, for nonlinear oscillations the minimum and maximum MB radius will vary with time (and cycle number) and the amplitude will deviate from the US excitation pattern [13].

Additional phenomena from MB stimulation by US can occur (see figure 1.1). Acoustic-forced oscillations of a MB can generate streaming of the surrounding fluid [20][21]. Fragmentation of a MB into smaller bubbles can occur at high pressures [22]. Acoustic radiation force from the US wave forces the displacement of the MB away from the transducer [23]. Pressures at which a bubble is unable

to withstand any further deformation (i.e typically $> 200kPa$) will cause the destruction of the bubble. This is called inertial cavitation [11]. The destruction of a bubble is paired with the emission of a high intensity, broadband US signal and can produce shock waves. Forcing the inertial cavitation of a MB can offer numerous theranostic advantages. Finally, the growth or shrinking of a MB can occur through the exchange of gases across the bubble membrane with the surroundings [24][25]. These phenomena are known as growth and dissolution respectively. At acoustic pressures just below the fragmentation (destruction) threshold, a MB will undergo dissolution wherein a small volume of the gas core escapes with each cycle of US [12]. MBs that experience growth or dissolution are characterized through a steady increase or decrease (respectively) of the backscatter amplitude for a long-cycle pulse of US.

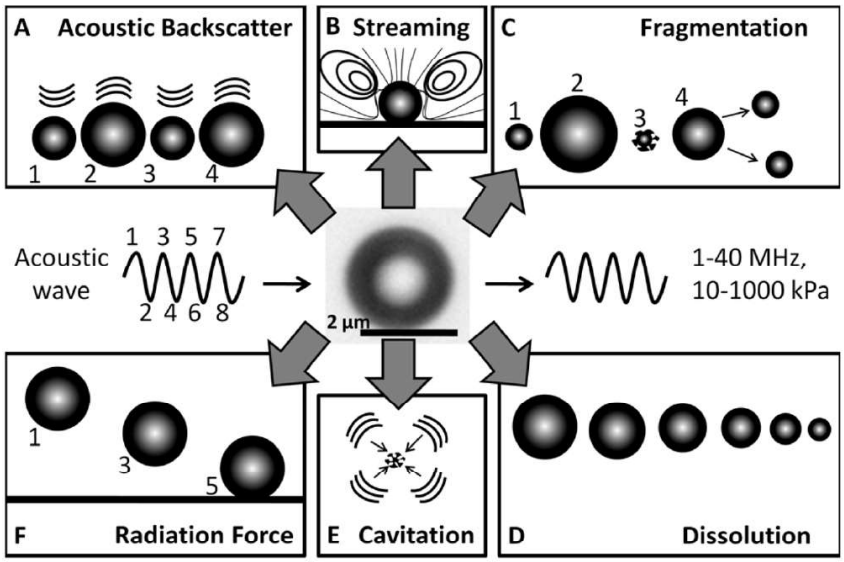

FIGURE 1.1: Variety of dynamic MB behaviours. Adapted from [12]

The parameters of a bubble behaviour occurring can differ for a bubble of different constitution.

Shell Effects

For a free bubble, the surface tension between the gas:liquid interface, the hydrostatic pressure or the acoustic pressure induces diffusion of gas from the core into the surrounding liquid. As a result, free gas MBs dissolve within seconds after having been introduced in the blood circulation [10]. The constitution of a MB can vary in terms of gas core and shell surfactants in order to extend the lifetime of the bubble for clinical use. The diffusion of a gas from a MB core is inversely proportional to the square root of its molecular weight. Therefore, MB cores with higher molecular weight will exhibit lower solubility or diffusion of the gas [10]. It is for this reason that the newest generation of contrast agents contain gases with high molecular weight, such as perfluorocarbons. Even MBs that employ a gas with high molecular weight can experience diffusion of the gas. An outer shell made up of surfactants (i.e proteins, polymers or phospholipids) can be used to remedy this. Surfactants act to decrease the surface tension of the gas to surroundings. This stabilizes the MB and further limits the loss of gas from the core.

Some formulations for MBs are commercially available for clinical use. MBs in the United States of America are currently FDA (Food and Drug Administration) approved for use in echocardiograms and liver imaging. The approval of US contrast agents is specific to the country in which they are used and the type of agent. Currently the only two FDA-approved, commercially produced agents in the US that are still in production are: Optison ™ (Mallinckrodt, San Diego, CA, USA) and Definity ® (DuPont Pharmaceuticals Co., NorthBillerica, MA, USA) [26]. The two formulations utilize albumin and phospholipid encapsulation, respectively. In Canada, Definity ® and Lumason ® are approved. Current commercially available agents like Definity ® (phospholipids), and Lumason ® (lipid) are all coated with a

shell.

The unique dynamical behaviour of the bubble is, in large part, owed to the malleable, deformable shell. With the addition of a MB coating comes dampening of the vibrations of the MB and changes to the MB resonance frequency. The shells of MBs, therefore, play a vital role in the behaviour of the resonant bubble system. For instance, the resonant frequency of a bubble is determined by the initial radius and shell elasticity. There are several theoretical formulations estimating the dynamic response of a MB and its resonance frequency [27][11]. The different theoretical formulations aim to account for the breadth of parameters by which a bubble can differ (ie: shell elasticity, surface tension, bulk modulus, bubble radius). The linear resonance frequency of a free MB (Minnaert-frequency) is given by:

$$f_0 = \frac{1}{2\pi r}\sqrt{\frac{3\kappa p_e}{\rho}} \tag{1.3}$$

where r is the bubble radius, κ is the polytropic exponent of the encapsulated gas, p_e is the equilibrium pressure inside the bubble and ρ is the density of the agent [27]. The resonant frequency is inversely proportional to the radius of the bubble. For exmaple, the resonant frequency of an un-encapsulated MB with 2μm diameter is 3.8 MHz while 9.4 MHz at 1μm diamenter. In comparison, the commercially available agent, Albunex (Molecular Biosystems, Inc., San Diego, CA, USA) has a resonant frequency of 45 MHz at 2μm diameter [11]. This is because the surrounding shell causes an additional restoring force during the expansion phase that is not present for a free bubble.

It is well established that the oscillations of the MBs are highly dependent on the shell parameters of the agent. When comparing a free bubble (no shell) to

a shelled bubble, and a stiff-shelled bubble, the increased elasticity in the encapsulating shell changes the resonance frequency of the MB and the viscosity of shell increases the damping of the vibration [10]. This asymmetric radial motion leads to an increase in harmonic scattering that is measured in the power spectra of the radiated sound pressures. The shell causes an increase in resonance frequency due to its stiffness and an increase in damping due to its viscosity. The material properties of the encapsulating shell on MB dynamics also shifts the pressure ranges where linear and nonlinear behaviours would be expected and may differ from agent to agent. The influence of the coating plays a key role in characterizing the behaviour of MBs.

Beyond Microbubbles: Less is more

MBs have several main limitations which vary in import depending on their desired application. The morphology of microvasculature is a signature of many diseases, including cancer. In tumours, the aggressive growth of the neoplastic cell population and associated overexpression of pro-angiogenic factors leads to the development of disorganized blood vessel networks that are fundamentally different from normal vasculature (i.e leaky) [28][29][30]. In the context of vascular imaging and cancer detection, MBs are restricted to the microvasculature, and therefore are less effective as theranostic agents for less vascularized tissue. For example, MBs are unable to penetrate to necrotic cores of tumour. Even in the case of a leaky vasculature where cellular gaps in vessel walls of tumours are enlarged through the enhanced permeability and retention effect [30], MBs are too large. For this reason nanobubbles (NBs) have been investigated. Bubbles are considered NBs if they have a diameter smaller than 1 μm. Though the area of research is relatively

new (2008) [31], NB research is garnering increasing interest [8][32]. To extravasate to the tumor itself, bubbles need to be smaller than 400 to 800nm in diameter [33]. The NB capacity to extravasate beyond the vasculature is greater than that of the MB due to small size. This extends retention of NBs in the target tissue.

At Case Western Reserve University (Cleveland, OH; Dr. Agata A. Exner), ultra-stable lipid NBs were developed that were able to maintain longer periods of contrast under ultrasound exposure than commercially available MBs [32]. The NB formulation features a shell containing a base lipid structure with two additives: propylene glycol (PG) and glycerol (G) that increase overall stability and applicability of these bubbles. Figure 1.2 is prvoided for a visualization of the shell architecture as designed by Exner et al. In vitro and in vivo experiments done by this group showed NBs to have higher echogenicity in vitro and slower decay rates in vivo compared to Definity ®[32].

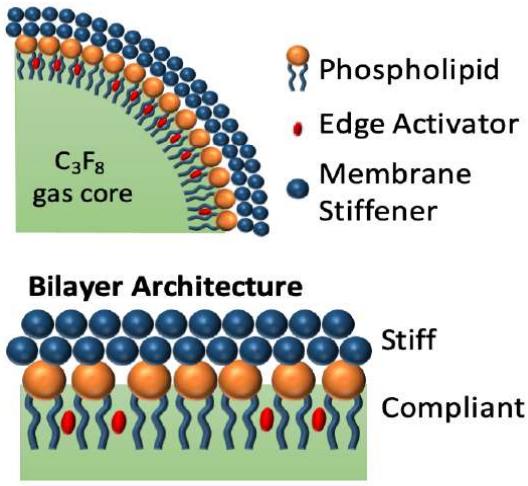

FIGURE 1.2: NB shell architecture (Edge Activator = propylene glycol; Membrane Stiffener = glycol). Adapted from [34]]

MB formulations are polydisperse, often with a subpopulation on the nano scale. This suggests that NBs can exhibit many of the same dynamical behaviours

as their larger counterparts under US stimulation. Definity ®MBs, for instance, are suspected to have a large NB subpopulation [35]. Furthermore, despite the tendency of larger bubbles to influence the dynamic behaviour of smaller neighbouring bubbles through bubble−bubble interactions [36], isolated NB populations have shown many of the same dynamical features, including inertial cavitation and harmonic content [8]. Like MBs, NBs can offer enhanced contrast in US imaging. Their primary advantage over MBs is their ability escape leaky vasculature (see figure 1.3). Figure 1.3) illustrates the passive targeting enabled by leaky vessels caused by abnormalities in tumour cell shape (shown by darker, overlapping cells), and cell packing. Abnormal cell shape can cause gaps in tumour-associated endothelium cells (light coloured, elongated, rectangular cells) lining blood vessels as compared to healthy endothelium cells (purple, elongated, rectangular cells) neighbouring healthy tissue (circular, light couloured called). In figure 1.3), normal tissue and normal endothelium is shown on the left; tumour tissue and associated endothelium is on the right.

1.2 Photoacoustic Imaging: Fundamentals

The photoacoustic (PA) effect was first discovered in 1880 by Alexander Bell. However, implementation of photoacoustic theory in biomedicine and imaging took hold in the late 1900's after the first use in tissue imaging by Browen in 1981 [37]. Developing side by side with optical and acoustic imaging modalities, PA imaging is now a fast growing and greatly maturing area of study in biomedical imaging [38].

In PA imaging, incident laser light guided by optical fibers illuminates a

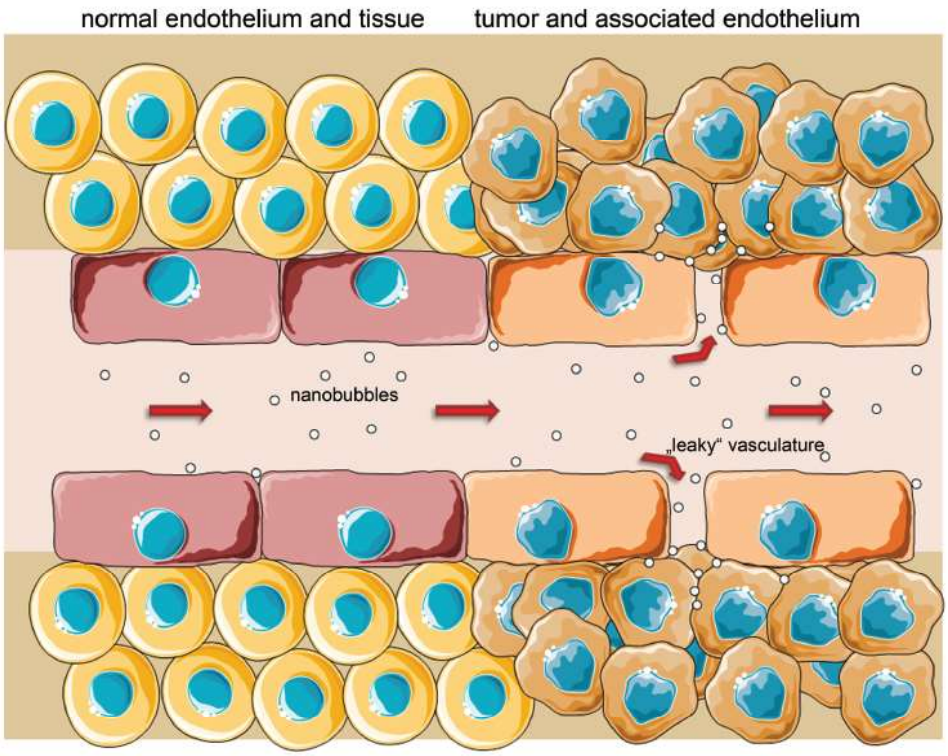

FIGURE 1.3: NBs in leaky vasculature. Adapted from [33]]

medium. Absorption of the infrared or near infrared light along the transport path is quantified by the absorption coefficient of an absorbing material. The absorbing molecule, or fundamental unit of material that absorbs, is called a chromophore. When the laser pulsewidth is limited by thermal and stress confinement conditions, the generation of an acoustic wave may occur as a result of absorption of the laser light by a chromophore [1][39][40]. This process can be modeled through the function:

$$p_0(r) = \Gamma \mu_a(r) \phi(r; \mu_a, \mu_s, g) \tag{1.4}$$

where the generated pressure wave p_0 at a radial distance r from the chromophore is expressed as a function of the Grüneisen coefficient, Γ, the absorption coefficient, μ_a, the fluence ϕ, the scattering coefficient μ_s, and the anisotropy factor g [1][40].

Thermal and stress confinement conditions are necessary for the efficient generation of a PA wave. Thermal confinement describes the condition that the laser pulsewidth must occur in a time length less than the thermal relaxation time. Thermal relaxation time characterizes thermal diffusion and is estimated by:

$$\tau_{th} = \frac{d_c^2}{\alpha_{th}} \tag{1.5}$$

where α_{th} is thermal diffusivity and d_c is the smaller magnitude between: dimension of the structure of interest or the decay constant of the optical energy deposition as discussed in [40]. To satisfy stress confinement conditions, the laser pulsewidth must be shorter than the stress relaxation time. Stress relaxation time characterizes pressure propagation and is estimated by:

$$\tau_s = \frac{d_c}{v_s} \tag{1.6}$$

where v_s is the speed of sound in the absorbing structure.

Electromagnetic radiation interacts with matter by scattering, absorption and transmission. As light propagates through a medium, these interactions with matter occur along the light path, and decrease the light intensity incident on the region of interest (ROI). As a result, the ROI experiences a reduced light intensity. Models that attempt to describe the transport of electromagnetic waves through

tissue account for the probability of photon interaction along the path length, and therefore reflect a reduction in power as a function of distance.

In the low frequency region of the electromagnetic spectrum, light experiences high penetration and low scattering. This window of high penetrance and low scattering is know as the 'optical window' and specifically refers to the infrared and near infrared regions ranging from approximately 600nm to approximately 900nm [41]. The "therapeutic" or "diagnostic" window extends this range to approximately 1300nm [42]. As a result of the behaviour of light in the diagnostic window, and the typically small angled geometry of the laser relative to the object surface, nearly 100% transmission through the interface occurs. The reduction of light intensity at the surface in acoustic resolution PA imaging is considered negligible.

The scattering and absorption coefficients describe the probability of a scattering or absorption event per unit infinitesimal length [38][40][43]. Both absorption and scattering coefficients are wavelength dependent, and tend to be larger for molecules of larger cross section and smaller for molecules of smaller cross section. The change in number of photons in depth is therefore dependent on the:

1. the loss of photons due to scattering in directions away from the main path trajectory
2. the gain from photons scattered from other directions into the field of view
3. the absorption of photons along the path length

In practice, Monte Carlo simulation methods are employed to simulate the

scattering and absorption interactions described above as a function of the probability of occurrence of interaction [43]. The overall effect is the attenuation of the incident light intensity. This attenuation reduces the fluence on the ROI and therefore, from equation (1.4), will reduce the amplitude of the generated pressure wave.

Only absorption interactions of the incident electromagnetic energy result in signal in PA images. Measures of the absorption coefficient in the human body vary greatly and can be interpretted through the definition provided in equation (1.7) where T describes the dimensionless surviving fraction of the incident light after an incremental pathlength L [44].

$$\mu_a = \frac{1}{-T}\frac{\partial T}{\partial L} \tag{1.7}$$

Water, blood, and fat content in tissue, to name a few, all have a different absorption spectra because of their differing molecular compositions. In the human body, percentages of absorption properties of contributing constituents for a tissue can act as an estimate for the net absorption coefficient of that tissue. The optical properties of varrying biological tissues have been previously investigated and summarized in depth [43][44].

After the chromophore absorbs the electromagnetic energy, the energy undergoes a conversion process. The thermal conversion efficiency η_{th} describes the percentage of absorbed photon energy that is converted into heat. The local pressure rise immediately after the laser pulse is proportionally related to η_{th} by:

$$p_o = \frac{\beta}{\kappa_i \rho C_V}\eta_{th} A_e. \tag{1.8}$$

Here, β is the volume thermal expansivity, ρ denotes the mass density of the chromophore, C_V represents the specific heat capacity of the chromophore at constant volume, A_e is the specific optical absoption, and κ represents the isothermal compressibility expressed by:

$$\kappa_i = \frac{C_P}{\rho C_V v_s^2}. \tag{1.9}$$

C_p is the specific heat capacity at constant pressure.

From heat, the energy undergoes a second conversion to mechanical energy. The Grüneisen parameter Γ is a dimensionless coefficient that describes the conversion of thermal energy into mechanical energy [38][1]. The Grüneisen parameter is given by:

$$\Gamma = \frac{\beta v_s^2}{C_p} = \frac{\beta}{\kappa_i \rho C_V} \tag{1.10}$$

A larger Grüneisen coefficient describes a chromophore that is more efficient at converting thermal energy to mechanical energy. At room temperature (22 °C) Γ is approximately 0.12 for water, approximately 0.16 for blood and approximately 0.8 for fat [38][45]. Γ is also dependent on temperature [39][40]. With water constituting 50-70% of body mass in humans it is reasonable to use the temperature dependence of water as an example [40][45]. Each millikelvin temperature rise in water or a high water-content medium (Γ of 0.2 at 37°C) will experience a 800 Pa pressure increase [45]. For every °C increase, the PA signal as a result of Γ increases by approximately 5%.

From this point forward PA physics are completely described by acoustic interactions. Optical absorption directly effects the initial amplitude of the generated ultrasonic wave, which, after some period of propagation, is measured by a

passive US transducer [2][46]. The propagation and detection of the acoustic wave describes the remainder of the physical process that occurs in PA imaging. After this point, conventional US technologies and methods can be used to reconstruct the information into images.

PA imaging has been developed and used in various and scalable operating modes ([38],[1],[47],[48]). Each operating mode exhibits a different set of attributes due to the setup of the system and lends to the scalability and versatility of the modality. Each mode will exhibit a different maximum axial and lateral resolution, and penetration depth (as shown in figure 1.4). The PA interaction can be used to image a large (approximately 1mm) vessel at depths a few centimeters deep as well as a vessel as small as 20 microns in diameter at depths of a few millimeters. To increase penetration depth, typically a transducer with a lower central frequency and therefore reduced lateral resolution is used compared to a system with a higher central frequency transducer with better spatial resolution [38]. PA imaging can therefore be used for a variety of scales with a variety of applications.

The underlying physical phenomena remain common among all PA modes, and are described by the same fundamental processes. The physics of the PA interaction can be summarized by three distinct stages:

1. **The optical stage:** from laser to medium and through the processes of optical refraction, transmission, scattering and absorption which subsequently causes thermomechanical effects

2. **The thermal stage:** from absorption to conversion of heat into mechanical energy and generation the ultrasonic wave

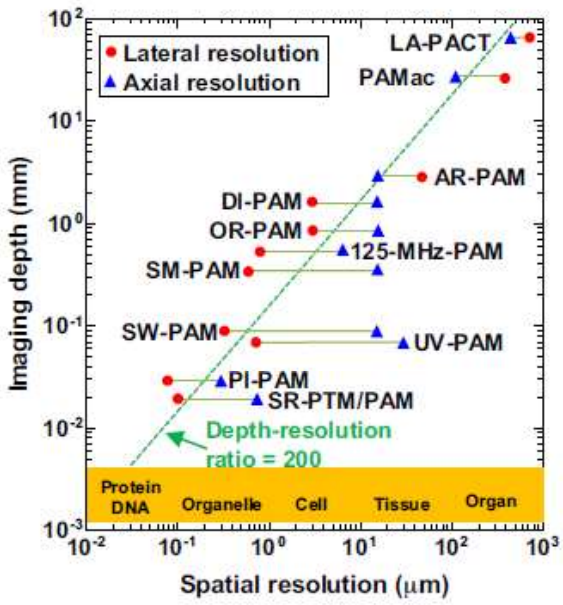

FIGURE 1.4: Acoustic resolution photoacoustic microscopy (AR-PAM) resolution compared with other PA modalities. Red circles denote lateral resolution and blue triangles denote axial resolution. Adapted from [38]

3. **The acoustic stage:** from generation through propagation of the ultrasonic wave (involving acoustic attenuation and scattering) to final detection

Each stage has an associated efficiency due to energy losses that ultimately limits the final sensitivity of a PA imaging system [38]. The definition of detection sensitivity is adapted from Yao and Wang as being an indicator of, "the minimum number of targets at different length scales needed to measure signals above the noise and provide accurate diagnosis of disease". The sources of these efficiencies and limitations have been investigated in depth [38]. In the optical stage, the detection sensitivity of acoustic resolution PA is mainly affected by the incident laser fluence. In the thermal stage, the optical absorption coefficient and the Grüneisen coefficient are limiting factors. In the acoustic stage, the main limitation on sensitivity is the detection efficiency of the ultrasonic transducer.

Various methods can be employed to improve the detection sensitivity of PA. The following work focusses on the use of external agents.

1.2.1 Photoacoustic Contrast Agents

The number of photons available for initiating the PA effect significantly decreases with depth, which results in lower amplitude acoustic waves that may not be sensed by the transducer [3]. The addition of exogenous PA contrast agents allows for microscopic imaging with improved selectivity and contrast at a cellular and molecular level [49]. PA contrast agents are materials that are developed to intensify and improve the PA-imaging ability and quality, including resolution, contrast and penetration depth [50]. This is achieved through the alteration of the PA characteristics of local tissue environments.

The PA characteristics of local tissue environments can be manipulated in either the optical or thermal stages of the photoacoustic interaction [50]. For thermal interactions, the PA signal is most dependent on the Grüneisen parameter due to temperature dependence [51][52]. The body temperature of a healthy individual is (37 °C). This is the ambient temperature for the ROI in biomedical diagnostic applications. In order to generate higher signal through the Grüneisen parameter one would need to locally increase the temperature of the medium. Consistent implementation of this for clinical applications would prove difficult due to thermoregulation of the body by surrounding blood vessels and could potentially cause damage by denaturing proteins in the ROI if temperatures deviate greatly. For this reason, this work focusses on alteration of the optical characteristics of local tissue environments through the addition of agents with high optical absorption.

Generally, studies of PA contrast agents aim to focus on either:

- developing new agents to address the short-comings of existing agents or
- modifying existing agents for multifunctional use in PA

The development of new exogenous PA contrast agents has been achieved using inorganic nanoparticles [53], carbon-based agents [54][55], small molecules (dyes) [49], and macromolecular compounds [50][56][57].

Gold nanoparticles have dominated the field of metallic nanomaterial studies for PA imaging [53]. Overall, metallic nanomaterials exhibit larger optical absorption cross-sections than endogenous agents. It remains to be seen whether the use of gold nanoparticles in reaching extravascular targets is generalizable across disease types and to applications in healthy tissue with intact vasculature. Despite being inert by nature, the in vivo biomcompatibility of gold nanoparticles has not been unambiguously established [53][54].

Carbon based nanomaterials including nanotubes, nanodiamonds and graphene based nanomaterials have shown potential for PA imaging owing to their flexibility of synthesis and functionalization [55]. The optical properties can be tuned through changes to the tube structure. Carbon nanoparticles are generally limited by their broadband absorption profile and low molar extinction coefficient. Additionally, investigations of biocompatibility are limited.

Dyes have been employed as molecular PA contrast agents. They exhibit high structural diversity and allow the tuning of their absorption and PA properties due to nonlinear absorption potential [49]. Their small ($\sim$ angstrom) size allows for enhanced contrast through vascular permeability. Advances in the development of

molecular dyes for PA focusses on the absorption capabilities of the agent and the potential of nonlinear PA applications. Most small-molecule dyes must be actively targeted to gain specificity. Challenges associated with the use of small-molecule dyes include a low molar extinction coefficient ($< 3x10^5 M^{-1}cm^{-1}$) and low solubility [56][58]. Molecular dyes also exhibit a tendency to aggregate and photobleach. It is possible to address some of these challenges chemically, by attaching hydrophilic groups or other stabilizing groups. Overall their chemical flexibility also facilitates the creation of "smart" contrast agents [56] and the modification of existing agents for multifunctional use in PA.

1.2.2 Multimodal US/PA Contrast agents

PA imaging is used in conjunction with US and fluorescence imaging because of the acoustic detection and optical excitation paths: the images are co-registered naturally. Synthesizing multimodal contrast agents is an important step toward quantitative multimodal imaging that seamlessly integrates PA with other modalities.

To date, several contrast agents have been investigated for US/PA imaging. A successful agent to be used for both US and PA imaging must exhibit two key properties in comparison to surrounding tissue: (1) high acoustic impedance and (2) high optical absorption. These conditions limit US/PA multi-modal agents to absorbing materials with a gaseous core.

With increasing attention, the pairing of one or more of the discussed PA agent types with or as surfactants for US agents has been developed [59][60].

The agents that have been investigated have been:

1. Loaded PA nanodroplets as activatable bubbles

2. Loaded bubbles

The study of these agents is in its infancy and a comprehensive review to compare them has not been published before.

Photoacoustic Nanodroplets

PA nanodroplets (PAnDs) are typically perflourocarbon (PFC) agents which can be forced to undergo a phase change when mediated by an external optical energy source. Due to the controllable phase change, PA nanodroplets function as activatable contrast agents [61][62]. PFC compounds have a wide range of boiling points and can be mixed at different ratios for controllable phase shift and selective vaporization of the agent [63]. An agent of the PFC family typically absorbs little optical energy in the near infrared region and therefore needs a chromophore incorporated as a heating source [64]. With these agents, the phase change is PA triggered due to the high optical absorption and generates a detectable acoustic transient. The resulting vaporization provides gas for acoustic impedance differences and therefore, US contrast. Nanodroplets can be loaded with genes, drugs or optically absorbing nanoparticle agents. Droplets with a smaller size with higher vaporization threshold temperature tend to be more stable and recondense consistently after vaporization, enabling repeated vaporization of the agent and longevity for extended imaging times [65].

TABLE 1.1: PA Nanodroplets (PAnDs) - Summary Table

Absorber Material	**Absorption Peak of Absorber**	**Droplet Diam.**	**Yield**	**Cit.**
Silica-coated lead sulfide nanoparticles (PbS)	n/a	1-12 μm	n/a	[62]
Nile red dye	530 nm	3 μm	n/a	[67]
Indocyanine-green (ICG)	800 nm (conc. dependent)	0.6 μm	10^9 PAnD/mL	[61]
India Ink	flat spectra	0.475 μm	n/a	[68]
Gold nanorods	790 nm (tunable)	0.4μm	10^8 PAnD/mL	[69]
Perylene diimide (PDI)	650 nm	0.1135 μm	n/a	[70]
Zonyl FSP fluorosurfactant	650 nm	0.06 μm	n/a	[71]

Some previously developed PAnDs are summarized in table 1.1. The extent of nanoparticle loading and the overall droplet diameter can be controlled during the synthesis process through filtering and sonication [63]. High optical absorption coefficients within the diagnostic window (ie PbS: 4.31 $cm^{-}1$ at 1064 nm [62]) have been achieved. Additionally PAnDs were shown to produce significantly stronger PA signals through the vaporization process than does the mechanism of thermoelastic expansion [64]. More recent studies have focussed on using absorbers with narrow absorption peaks for selective activation of differently-coloured droplets [66]. Narrower agent absorption spectra give rise to the potential spectral unmixing of agent signal for uses in a wider variety of PA modes.

These agents were developed in the hopes of addressing some of the limitations of bubble agents, however they have limitations of their own. Narrow absorption spectra limit the wavelength at which agent activation can occur thereby

limiting range of systems with which the same agent can be used. Conversely, too wide of an absorption spectra makes spectral unmixing and other PA modes difficult to implement practically. Finally, because the agents are not FDA approved, translation to clinic may experience significant delays.

In a similar fashion to PFC nanodroplets, activatable MBs and NBs have been developed by adding shell and surfactant materials to a PFC emulsification. Prior to activation, droplets feature a surfactant shell encompassing a liquid PFC core; after activation the PFC core is vaporized and trapped within the surfactant-shell [63].

Multimodal Bubbles

MBs are a natural approach for US/PA agents due to their acoustic behaviour. The integration of existing PA agents into bubble shells or cores has been proposed to increase bubble optical absorption and enable optically-based contrast. Improved efficacy has been shown of some molecular imaging agents when functionalized with moieties targeted to specific molecules when compared to free untargeted agents. This was shown in the case of gold nanorods bound to the surface of microbubbles [60]. The main contenders for PA agents and their integration into bubble shells are (1) nanoparticles and (2) dyes. A comprehensive list of agents produced to date is summarized in table 1.2.

Visible in table 1.2, the integration of previously developed PA contrast agents into existing US MBs were used to increase the optical absorption of the MB based contrast agent. The bubble agents developed utilized a variety of shell materials and gases for the encapsulated core. Additionally, a broad spectrum of

TABLE 1.2: PA Bubbles - Summary Table: blue: nanoparticle absorbers; green: ink and dye absorbers; light green: MBs; bright green: NBs. (** as reported in manuscript)

Absorber Material	**Absorption Peak of Absorber**	**Shell Material**	**Core content**	**Bubble Diam.**	**Yield**	**Year**	**Cit.**
Gold nanorods	**760 nm	albumin	C_3F_8	5 μm	3.8E9 μB/mL	2012	[46]
Avidinated gold nanoparticles	525 nm	lipid	C_4F_{10}	4.5 μm	>1E7 μB/mL	2013	[72]
Graphene	flat spectra	polyvinyl alcohol	air	3.6 μm	3.5E8 μB/mL	2016	[73]
Gold nanorods	**750 nm	lipid	C_4F_{10}	n/a	n/a	2015	[60]
Black ink	n/a	lipid	N_2	9.73 μm	1E5 μB/mL	2018	[74]
Methylene Blue Dye	670 nm	lipid	N_2	4.72 μm	1E8 μB/mL	2018	[74]
Methylene Blue Dye	**667 nm	lipid	C_3F_8	3.5 μm	4.5E9 μB/mL	2014	[75]
Rose Bengal	560 nm	polymer	C_3F_8	2.75 μm	1E9 μB/mL	2014	[76]
Porphyrin	**700 nm (solvent dependent)**	lipid	C_3F_8 & C_4F_{10} & SF_6	2.7 μm	1-10E9 μB/mL	2012	[77]
Rose Bengal	560 nm	lipid	C_4F_{10}	1.7 μm	1E9 μB/mL	2012	[78]
Indocyanine-green	340 nm	lipid	C_3F_8	1.29 μm	n/a	2018	[79]
India Ink	flat spectra	PLGA	air	1.01 μm	n/a	2010	[3]
India Ink	flat spectra	PLGA	air	0.29 μm	n/a	2010	[3]
Sudan Black	600 nm (solvent dependent)	lipid	C_3F_8	0.17 μm	n/a	2018	[80]

bubble sizes have been generated where most agents are appropriately sized for vascular imaging. It is also promising that the methods of agent production generate high yields; where reported, the yield of the bubble agents tend to be on the order of $\sim 10^8$, similar to that of PAnDs. Finally, the majority of US/PA bubble agents developed have been produced in the last ten years, indicating that this is a burgeoning research area.

Nanoparticles from gold spheres [72], gold nanorods [60][69], and graphene nanosheets [73] offer large optical absorption necessary for initiating the PA effect. Dove et al. reported a stronger PA response from gold MBs than that observed from free nanoparticle solutions with the same nanoparticle concentration [72]. It was hypothesized that the high nano-particle concentration surrounding the compressible gas core allowed for laser energy to drive the resonant oscillations of the MB [72]. Similar results for another group were hypothesized to be a result of small NBs produced at the perimeter of the MB [60]. In this study, Dixon et al hypothesized that NB formation occured as a result of high local temperature increase. They also hypothesized that the gas core provided thermal insulation and therefore added directivity to the thermal deposition of the incident optical energy. Dove et al. also reported a minimal effect of nanoparticle loading on the MB b-mode and nonlinear ultrasound intensities. A large absorption cross section, such as that exhibited by gold nanoparticles, can lead to partial melting of the nanorods when irradiated [81]. The melting process forces a shape-change of the gold particles upon laser irradiation, and alters the absorbance peak of the agent, which can lower the photothermal conversion efficiency at the preset irradiation wavelength [70]. Moreover, in the presence of a lipid/polymer or protein shell, agents may be destabilized or destroyed. Finally, bioeffects (ie. biodegradation) of these agents are not well studied. Dyed agents can offer a safer and more stable alternative.

MBs ($\sim$1 μm) and NBs ($\sim$290 nm) loaded with India ink have been fabricated [3]. Made from the same protocol with a different filtration procedure, this study discusses the versatility of production methods for dyed agents. Gelatin phantom-embedded targets of India ink MBs and NBs were clearly visible by PA macroscopy even when a piece of 18 mm thick chicken breast tissue was placed between the targets and the optical source. These preliminary results suggest the technical potential of using ink-integrated MBs and NBs for quantitative photoacoustic and US imaging in thick biological tissue [63]. The relatively flat absoprtion spectrum of India ink, however, decrease the specificity of these agents in PA imaging.

Methylene Blue bubbles containing PFC gas were produced by sonication and mechanical agitation [75]. Methylene Blue is a cationic stain and binds to negatively charged parts of cells, such as the DNA and RNA. Methylene Blue is a common stain for a large number of targets including identification of bacteria, and delineation of cellular structure in both plant and animal cells. As a method of acoustic characterization, frequency-dependent attenuation measurements were performed using a narrowband pulse-echo method covering a frequency range of 1.5 to 12 MHz. No significant difference in the attenuation measurements of dyed and undyed bubbles was seen. For PA, their findings show that with an increase in number of MBs a suppression of PA signal while no US change is observed. Bursting the MBs corresponded with short term PA signal enhancement. The researchers also comment on the accessibility of the newly developed agents for clinical translation.

Recently, microfluidic methods of bubble production have been proposed. Das et al used a flow-focusing microfluidic device for the generation of two types of

PA-nitrogen microbubbles where (1) Methylene blue or (2) Black Ink provided optical absorption [74]. Microfluidic MB production of the two agents was succesful and produced relatively high yeilds, however Methylene blue MBs were produced at a significantly higher yield than Black Ink bubbles (see table 1.2). Differences in bubble yield may indicate instabilities caused by molecular interactions of the Black Ink with the lipid shell. Das et al also calculated signal to noise ratios (SNR) of both US and PA imaging experiments and compared for the two agent types. SNR in both US and PA were higher from Black ink MBs than Methylene Blue MBs. The discrepancy in US imaging SNR values of the Black Ink MBs and the Methylene Blue MBs was attributed to the complex wall interactions between the housing tubes and nearby Methylene Blue MBs [74]. Another factor which was not discussed in their report was the effect of the bubble diameter on US backscatter. Differences in SNR for PA were said to be negligible, however no mention of the effect of differences in optical absorption of the two absorbers at the stimulating wavelength was mentioned. Importantly, of the two agents produced, Methylene blue is a currently FDA approved dye and would be likely to see faster translation to clinic due to its rigorously investigated safety profile.

Similarly, Indocyanine Green (ICG) is one of the first optical contrast agents approved by the FDA for clinical imaging applications [63]. It is commonly used as a blood pool agent because of its strong binding to plasma proteins in the vascular system. The fluorescence emission peak of ICG falls in the near-infrared wavelength range, enabling deep penetration of light through thick biological tissue [63]. Encapsulating ICG in PLGA MBs has also yielded dual-mode contrasts for simultaneous US and PA imaging [79].

Rose Bengal is a biological stain that adheres to dying and degenerating

cells. It is a hydrophilic anionic photosensitizer. Rose Bengal MBs were developed for the use of sonodynamic therapy to enable delivery of rose bengal to the target site followed by its activation at that site. Rose Bengal sensitizer that was attached to lipid-stabilized MBs produced conjugates that displayed toxic effects against cancer cells both in vitro and in vivo upon exposure to ultrasound irradiation [78]. Similar polymer agents were produced that successfully addressed the need for conjugates with enhanced stability [76]. Although these agents were not originally proposed for US/PA imaging, the high absorption coefficient of the photosensitizer Rose Bengal makes the MB agent a potential contender for PA-triggered therapy.

Porphyrin is an end product of hemoglobin metabolism. Previously, the formation of phospholipid bilayer nanovesicles entirely from porphyrin-lipid conjugates with structure-dependent photonic properties were introduced as biophotonic contrast agents [82]. More recently, porphyrin-phospholipid conjugates were used to create MBs having a porphyrin shell, and their US and PA properties were investigated [77]. The inclusion of porphyrin-lipid in the MB shell increased the yield, improved the serum stability, and generated a narrow volumetric size distribution. Additionally, a theoretical approach was used to determine the MB shell elasticity (increased with porphyrin integration) and shell viscous effects were determined for the frequency range of 9-10 MHz as estimated by the resonance frequency expected for the diameter of their MB population. It was hypothesized that the increase in shell elasticity due to the porphyrin-lipid may contribute to the increased yield and serum stability over MBs formed without porphyrin-lipid [77]. These findings support the importance of investigating differences in acoustic properties upon the addition of new agents to the bubble shell.

Recently, Sudan Black NBs were produced. Sudan Black B has been used

for the sensitive and specific staining of phospholipids and intracellular lipids [83]. The formation of pores on the cell plasma membrane is known as poration. The process of poration can be mediated by external energy sources such as sound (sonoporation) or light (optoporation). In [80], a preliminary investigation on the use of Sudan Black B-loaded NBs (lipid shell) to facilitate optoporation of individual BT-474 cells that were targeted by the dyed NBs was proposed. Through the successful use of Sudan Black B dyed NBs as PA agents reproducible poration was achieved. No report, however, has been provided on the characterization of these agents. With potential as US/PA agents a more thorough characterization of the PA and US behaviours is needed.

Further improvement in process control and engineering optimization is required for the production of monodisperse agents with high encapsulation rate, productivity and reproducibility. Additional attention is needed for the strategic use of optical absorbers that are biosafe and affect the stability of the agent minimally. The impact on the acoustic response of the absorber integration in the shell needs to be investigated.

1.3 Thesis Overview

US/PA multimodal imaging is a promising tool for early tumor detection and diagnosis because of the vascular imaging capabilites of both modalities. It is desirable to produce a single contrast agent that can address the cases in which both US and PA modalities are used for biomedical imaging. Dyed bubbles can address photon loss with depth by increasing the optical absorption in the region of interest while simultaneously offering enhancement in US imaging through increased

echogenicity and nonlinear bubble behaviour.

1.3.1 Project Motivation

When MBs are injected into the circulatory system and stimulated with ultrasound at the desired location, the ultrasound wave forces nonlinear oscillations of the MB which are the main driver for effective contrast enhancement [15][16][17]. It is well established that the oscillations of the MBs are highly dependent on the shell parameters of the agent [15][17]. Previous approaches using coated US contrast agents did not rigorously investigate the effects of dye integration in the bubble shell on bubble dynamics or bubble stability in the context of US. Although Jeon et al briefly investigated the effects of methylene blue dye on bubble attenuation, there are several limitations to this study [75]. Firstly, the bubble attenuation represents the combination of effects of (1) attenuation by bubble backscatter (a.k.a bubble acoustic re-radiation) and (2) attenuation by acoustic energy damping. As a result, a peak in attenuation measurement does not equate to a peak in bubble backscatter. Secondly, the attenuation experiments that were conducted evaluated the bubbles at a single pressure (25 kPA; relatively low), for a very small frequency window (1-10 MHz). Considering the sensitive dependence of MBs to initial parameters, it is possible that molecular effects of the dye on the lipid shell are not detectable under the conditions that were tested. Thirdly, it has been suggested that a possible mechanism leading to increased MB stability is an increase in shell elasticity and decreased gas permeability[25], and that this can be altered with the presence of added absorbers in a bubble shell[77]. Finally, NB capacity to extravasate beyond the vasculature is greater than that of the MB due to small size. This extends retention of NBs in the target tissue and offers greater flexibility and sensitivity to cancer

for US/PA multimodal imaging..

Closer attention needs to be paid to the effect of added constituents to NB dynamics. If the process of integrating PA absorbers (dye) alters the NB shell properties, use in US applications without appropriate adjustments of incident acoustic parameters would result in suboptimal function. These effects remain underexplored.

Motivating Data

Propylene glycol and glycerol (PGG) bubbles with Sudan Black B dye were produced. Previous studies have estimated the organization of the shell constituents of PGG bubbles as shown in figure 1.2. It is expected that the integration of Sudan Black B into the lipid-shell formulation will destabilize the lipid shell of a NB. Sudan Black B is highly hydrophobic and is expected to line the internal portion of the shell closer to the ends of the hydrophobic tails. An approximate schematic of the organization of the shell is shown in figure 1.5.

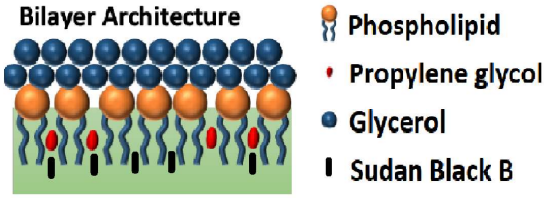

FIGURE 1.5: SBNB shell architecture. Modified from [34]

It is possible that the Sudan Black B organization in the lipid shell further separates the phospholipid tails. As the tails are further separated the already compliant shell would increase in elasticity.

Recently, a novel acoustic-based flow cytometer was developed and used to detect individual nanobubbles flowing in a microfluidic channel using high-frequency ultrasound and photoacoustic waves [84]. In this setup, the foci of high-frequency ultrasound (center frequency 375 MHz) and nanosecond laser (532 nm) pulses are used to generate ultrasound backscatter and photoacoustic waves from the same single agents as they are passed through the system. In this report, the average maximum amplitude of the US backscatter signals from at least 950 nanobubbles with an average diameter of 225 nm was nearly half that from Sudan Black-B dyed NBs (SBNBs). Additionally, this published work shows bubbles with the dye in the shell suppressed unique features seen in the time−domain ultrasound backscatter from the nanobubbles without dye.

Figure 1.6 shows one representative RF-line from each NB type, undyed (mean diameter $= 225\ nm$) and dyed with Sudan Black-B (SBNBs) (mean diameter $= 238\ nm$). After threshold filtering, from 100 RFlines, 100 power spectra were obtained and averaged for the undyed and dyed NBs. This data is presented in the rightmost pannel of figure 1.6.

Several key differences are visible when comparing the data of undyed NBs and SBNBs in the frequency domain. At the center frequency of the transducer (375 MHz), where the transducer is more sensitive to linear bubble behaviour, SBNBs express higher power than undyed bubbles. Bubble activity from undyed bubbles increases at frequencies away from the center frequency of the transducer, suggesting nonlinear activity. The SBNBs do not show peaks away from the center frequency of the transducer and therefore, appear to behave in a more linear manner than their unchanged counterpart; this can be a consequence of increased shell elasticity. Overall, this data suggests that the contribution of Sudan Black in a

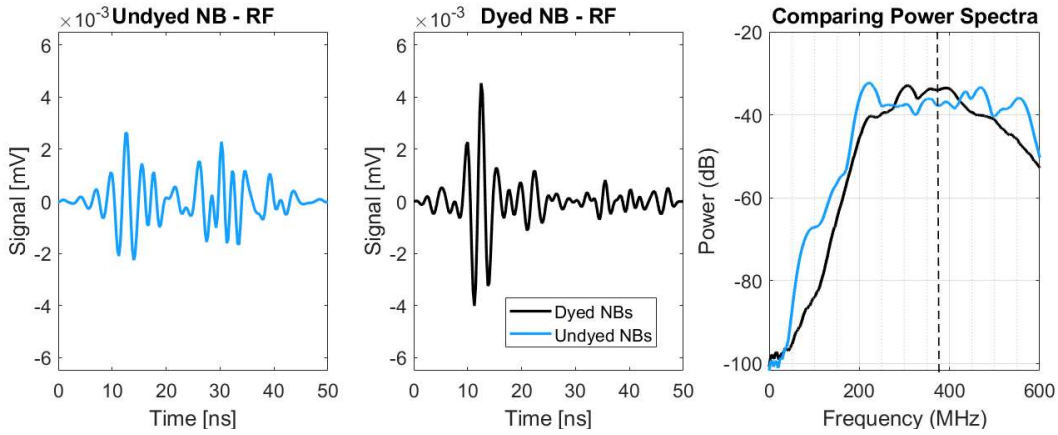

FIGURE 1.6: (a) A single representative RF line of an coustically excited nanobubble; (b) A representative RF line of an acoustically excited, Sudan Black dyed nanobubble; (c) A comparison of 100 averaged power spectra for dyed and undyed nanobubbles

bubble shell can alter the acoustic signature of the NB.

Hypothesis and Specific Aims

Hypothesis

The integration of Sudan Black B dye into the lipid-shell of a NB affects the bubble dynamics in response to ultrasound as a result of changes to the physical properties of the bubble shell.

Specific Aims

The specific aims of this work are:

1. Produce nanobubble formulations with varying Sudan Black B content
2. Visualize bubbles, test production yield and determine bubble size distribution
3. Test bulk shell-material surface tension
4. Test acoustic bubble response for single bubbles and bubble populations
5. Demonstrate simultaneous ultrasound and photoacoustic multimodal contrast

Chapter 2

Methods

2.1 Contrast Agent Production and Validation

2.1.1 Lipid Sample Preparation

All bubble samples were produced in-house. The base protocol for the production of ultra-stable propylene glycol with glycerol bubbles (PGG bubbles) used for the current work was previously published [34]. The protocol with the addition of Sudan Black differs minimally from the published work.

The lipids 1,2-dibehenoyl-sn-glycero-3-phosphocholine (DBPC), 1,2-dipalmitoyl-sn-glycero-3-phosphate (DPPA), and 1,2-dipalmitoyl-sn-glycero-3-phosphoethanolamine (DPPE) were obtained from Corden Pharma (Switzerland), and 1,2-distearoyl-sn-glycero-3-phosphoethanolamine-N-[methoxy(poly(ethylene glycol))-2000](mPEG-DSPE) (ammonium salt) was obtained from Laysan Lipids (Arab, AL). All materials were used as received. When not in use, lipids were stored at -20 °C.

TABLE 2.1: Lipid Shell Components

Material	**Amount**
DBPC	60.1 mg
DPPA	10 mg
DPPE	20 mg
DSPE-mPEG	10 mg
Propylene Glycol	1.03 g
PBS	8 mL
Glycerol	1 mL

Prior to use, lipids were set to rest at room temperature for 15 min. A water bath was prepared at 80 °C for later use. A sonicator (1510 Branson, Branson Ultrasonics Corp., CT, USA) was filled with deionized water at 22 °C, also for later use. Glycerol (Acros Organics, NJ) was lightly mixed and dissolved into phosphate buffered saline (PBS) (Wisent Bioproducts, QC, Canada) and set aside at room temperature.

Lipids were measured according to the protocol in [34] and as listed in Table 2.1 and placed in a 20 mL glass vial (Fisherbrand, PA, USA). Each lipid type was measured separately on weighing paper (Fisherbrand, PA, USA) using an enclosed electronic scale (Scientech, CO, USA). Propylene Glycol (PG) was added to the lipids and placed under 80 °C in the water bath for 30 minutes or until a homogeneous solution of dissolved lipids in glycerol was achieved.

Sudan Black B (SB) dye (Sigma Aldrich,) was measured in amounts of 0, 1, 2, 3, 4, or 5 mg on weighing paper and added to dissolved lipid-PG solution. SB was fully dissolved in lipids under heat. The 20 mL vial containing the lipid-PG-SB solution was intermittently swirled and replaced into the hot water bath until there were no visible precipitates remaining. The PBS-glycerol mixture was heated to 80 °C in the water bath. When both solutions, lipid-PG-SB and PBS-glycerol solutions

reached 80 °C the PBS-glycerol mixture was added 1 mL at a time followed by swirling into the lipid-PG-SB solution. When the full 9 mL volume of PBS-glycerol was added and lightly mixed into the lipid solution, the vial was sonicated for 15 min. The final 10 mL yield was aliquoted into ten 1 mL aliquots in 1.5 mL vials and sealed by a rubber cap.

The final vial yield following this protocol was 60 vials of 1 mL lipid solution with 10 vials of 1 mL for each SB measurement (see fig 2.1). The final SB concentration in the vials was 0, 0.1, 0.2, 0.3, 0.4, or 0.5 mg SB per 1 mL lipid solution (see fig 2.1 and 2.2).

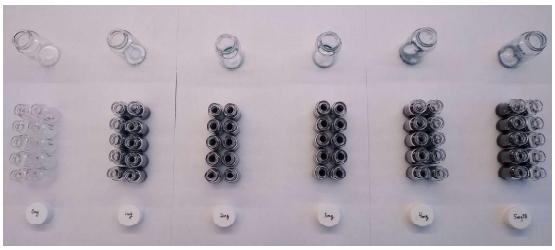

FIGURE 2.1: Sudan Black Nanobubble Alliquots

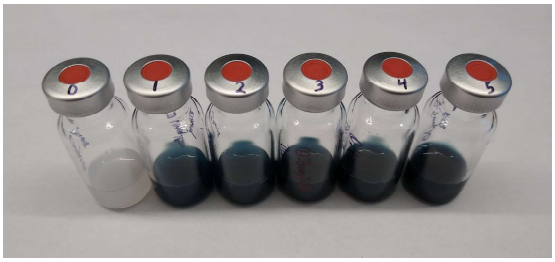

FIGURE 2.2: Final SBNB Vials - 1 mL Alliquots

2.1.2 Nanobubble Activation and Isolation

Internal gas was exchanged in order to prepare the vials for bubble activation. Briefly, a 25G needle (Becton Dickinson (BD), NJ, USA) attached to a 20 mL

syringe (Becton Dickinson (BD), NJ, USA) was used to remove gas from the vial. This was repeated 6 times. A 10 mL syringe (Becton Dickinson (BD), NJ, USA) with a 25G needle attached was filled with octafluoropropane (C3F8) (Synquest Labratories, FL, USA). Using this filled syringe the vial was punctured through the rubber seal. The rubber seal was then punctured with a second needle for venting and the octafluoropropane-filled syringe was depressed into the vial. Both needles were removed from the vial to complete the gas exchange process.

To activate the lipid solution, the bubble vial was shaken using a Vialmix (Bristol Myers Squibb(BMS), NY, USA) mechanical shaker for 45 seconds. After shaking, the vial was inverted and centrifuged (MXIE TD5A-WS) for 5 min at 50 rcf (550 rpm). After centrifugation the vial was kept inverted during the sample draw to limit mixing of activated bubbles and help control for bubble size distribution. To collect the sample from the bubble vial, the penetration depth of the 18G needle into the vial was controlled by cutting a needle cap such that when placed over the needle. Only 5 mm of the needle tip stuck out. Without inverting the vial, using an 18G needle (Becton Dickinson (BD) with cut cap and a 1 mL syringe 300 μL of activated bubbles was drawn from the bottom of each vial. This 300 μL was used as activated stock bubble solution.

2.1.3 Bubble Filtration

For filtered bubble samples, activated stock bubble solution was diluted in PBS in an 1:9 dilution and was used to fill a 3 mL syringe. A single use filter unit (FroggaBio, ON, Ca) with 450 nm pore size was attached to the tip of the 3 mL syringe. The syringe was depressed by hand at a rate of $\sim$1 droplet per 5 seconds

until there was no remaining fluid. The refuse was collected by a 5 mL centrifuge tube for later use.

2.1.4 Transmission Electron Microscopy

TEM images of the bubbles were obtained using a FEI Tecnai G2 Spirit BioTWIN TEM operated at 120 kV based on a previously reported method [85]. A dilute suspension of the sample (10 uL) was placed upside down on a 400 mesh Formvar-coated copper grid. The sample was then stained with 2% uranyl acetate after which the sample was allowed to dry for 30 min.

2.1.5 Bubble Sample Validation - Concentration and Size

Bubble vials of each sample type (0 mg/ml, 0.1 mg/mL, 0.2 mg/mL, 0.3 mg/mL, 0.4 mg/mL and 0.5 mg/mL SB) were activated. From the stock solution, a 1 in 500 dilution of activated bubbles was prepared for each sample type in PBS and sized using the Archimedes resonant mass measurement (RMM) system (Malvern Panalytical, MA, USA) (figure 2.3). RMM has been established as a successful technique for counting and sizing of suspended buoyant and non buoyant particle types [86]. A microfluidic pathway flows particles past a resonating cantilever (see figure 2.3b)causing a measurable shift in frequency proportional to the size and density of the particle. Using RMM, buoyant-particle concentration and diameter of the 1 in 500 dilutions were determined. Filtered bubbles were prepared in 1 in 10 dilutions due to bubble destruction caused by the filtration process. This process was repeated three times for each sample type (see Appendix A for sample distribution curves).

(A) System

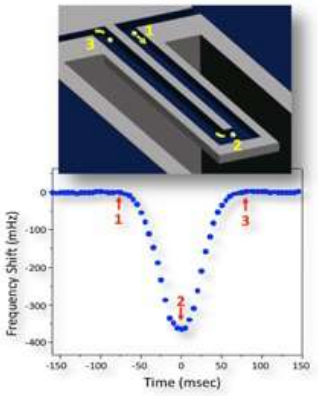

(B) Resonating cantilever with an example of frequency shift caused by a passing particle

FIGURE 2.3: Archimedes Resonant Mass Measurement System. Adapted from [87]

2.2 Testing Shell-Material Properties

Shell material properties were estimated by measurement of the bulk lipid material without bubble activation.

2.2.1 Surface Tension

A CAM 200 optical goniometer by KSV Instrument, Ltd. with a pendant drop tensiometry setup was used to measure the surface tension of the various sample types at a lipid to air interface. A flat tipped needle (0.48mm O.D.) was used. In pendant drop tensiometry, gravity is responsible for the deformation of the sample. The deformation is used to quantify interfacial tension through a fitting algorithm to the Young-Laplace model. In order to maximize the deformation caused by gravity on the droplets and to obtain the most accurate results [88], samples were extruded from the needle to hold the largest possible, stable droplet (sample

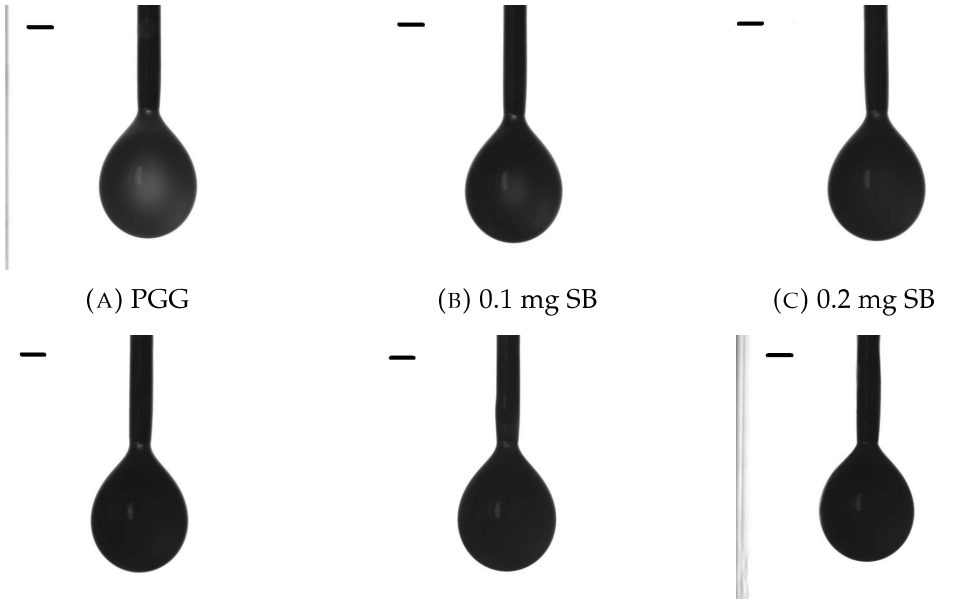

(A) PGG (B) 0.1 mg SB (C) 0.2 mg SB

(D) 0.3 mg SB (E) 0.4 mg SB (F) 0.5 mg SB

FIGURE 2.4: Lipid solution Pendant droplets for surface tension measurements; (scale bar = 0.5251 mm)

droplet images provided in figure 2.4). Water was used for accurate calibration of the system. Measurements were collected at 22.3 +/- 0.3 °C.

2.3 Single Bubble Acoustic Stimulation

2.3.1 System

The acoustic stimulation of single SBNB agents was studied using the Vevo 770 US system (figure 2.5). A focussed RMV-710B transducer (f-number 2.1; aperture 7.14 mm; focal length 15 mm) with center frequency of 25 MHz and 100% bandwidth was used. This transducer has a mechanical scan head which oscillates laterally as it scans a fixed region of interest as defined by the specifications outlined

in Table 2.2.

FIGURE 2.5: Vevo770 System and RMV-710B focused transducer in a beaker of 500mL water. Adapted from [13]

TABLE 2.2: Single-Bubble ROI Specifications

Specification	**[mm]**
Depth	14.57
Length	3.29
Position	6.24
Width	0

Bubbles were stimulated with 30 cycle pulses at 25 MHz at varying pressures controlled by % transducer power. Exact pressures used are shown in table 2.3. Calibration of the US transducer was done in a previous study [89]. For each power setting, 25 data sets were collected. Each data set contained 100 RF lines where one RF line represents the measured backscatter data associated with the material along the axial path of the transducer. A total number of 12,500 RF lines were collected for the 0, 0.2 and 0.4 mg SB samples. This experiment was repeated three times from three different vials of the 0, 0.2 and 0.4 mg SB samples.

TABLE 2.3: Single Bubble Ultrasound Pressures

% Transducer Power	Pressure [MPa]
6	0.2
20	0.6
32	1.0
63	2.0
100	3.0

2.3.2 Experimental Setup

An activated and filtered bubble solution was used. Immediately after filtering, the Archimedes system was used to determine the bubble concentration (Aconc). Using the dilution-corrected Archimedes concentration (Aconc*Dil), the volume of nanobubbles (V) was determined such that, when added to a 500 mL volume of DI water, a final concentration of $\sim$ 2000 NBs/mL was produced. This was calculated through:

$$V = \frac{2000NBs}{1mL} \cdot (500mL) \cdot \frac{1}{Aconc * Dil} \frac{1E3\mu L}{1mL} \tag{2.1}$$

Five beakers, each containing 500 mL deionized water were prepared and allowed to rest for 15 min at room temperature. The volume V as determined above was added to one of the five beakers of DI water. The diluted solution was gently stirred to disperse the bubbles. The transducer head was submerged into the beaker and held in place 3 cm below the surface of the water by a clamp. A new dilution with the same solution volume was prepared for each pressure of the transducer to ensure high numbers of measurements that were concentration independent.

2.3.3 Data Analysis

RF data from the VEVO 770 system was exported and saved for further analysis. Analysis of the data was executed in Matlab R2019b. Base code for data analysis was adopted from previously developed methods [13]. Those methods are summarized here, in brief.

All RF lines from all data sets were stored and saved in an array. To prepare the data for analysis, the RF data was converted from time to frequency domain through application of the fast fourier transform. This yielded the power spectra of the data. Attenuation effects were accounted for based on expected frequency-dependent attenuation effects of an acoustic wave travelling in water by multiplying the signal by a correction factor determined by the expected attenuation experienced as a function of distance from the transducer. The data was then ready to be passed through a set of criterion for classification as single bubble signals.

RF lines lacking bubbles, truncated RF lines, or lines wiht signal from more than one bubble were removed. Signals that had a maximum peak below a 0 dB threshold in the power spectra were interpreted as RF lines lacking bubbles and were therefore discarded. By ensuring that the first and second peaks, as well as the last and second last peaks found in the RF line (time domain), fell below a bubble threshold of 50% of the max peak of that RF line, truncated signals were identified and removed. Additionally, RF lines that had 33 or more peaks above 50% of the power spectra max were determined to have excessively high noise or more than one bubble and were discarded. Finally, a peak to peak noise threshold comparing the non-bubble portion of the RF line to the noise threshold for each particular experiment was set as 2.5. Signals above this threshold were interpreted as having

more than one bubble and were discarded. Remaining signals that passed these criteria were displayed for viewing and classification.

Accepted signals were classified as either linear or nonlinear responses. A linear oscillation has a minimum and maximum radius that is consistent throughout most of the oscillation. Such signals were labelled **p1**. In some cases, linear signals occurred such that a steady increase or decrease in amplitude with cycle number was detected. Such signals were labelled as $p1_{growth}$ or $p1_{diss}$ respectively. Samples of linear signals are shown in figure 2.6.

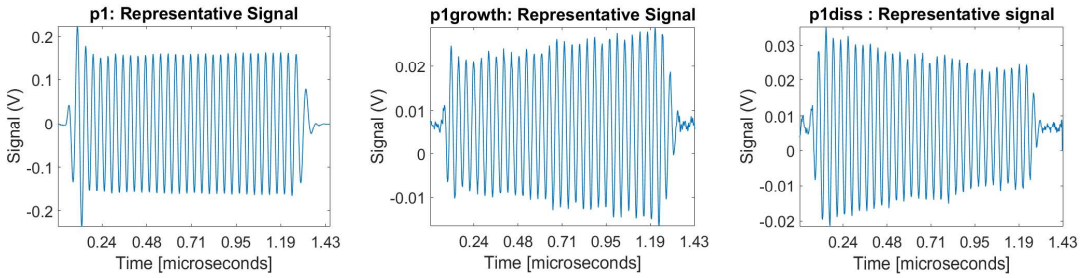

(A) $p1$ (B) $p1_{growth}$ (C) $p1_{diss}$

FIGURE 2.6: Representative signals for linear oscillations

Nonlinear signals could show consistent patterns in integers (every 2 peaks; every 3 peaks; every 4 peaks) and thus were labelled **p2, p3, p4, p5, p6** or **p7** depending on the pattern observed. The signal was classified based off of the most commonly occurring repetitive sequence in the RF line. For some signals, there is no obvious pattern in oscillation. There is evident nonlinearity due to the different heights in peaks of RF lines however there is not a reliable, repeatable sequence. These signals have been denoted **px**. Samples of nonlinear signals are shown in figure 2.7. For signals were only a subset of the cycles exhibit the periodic behaviour, a red box is used to indicate where the periodic behaviour can be viewed.

In some cases, the signal demonstrated a bubble that does not complete

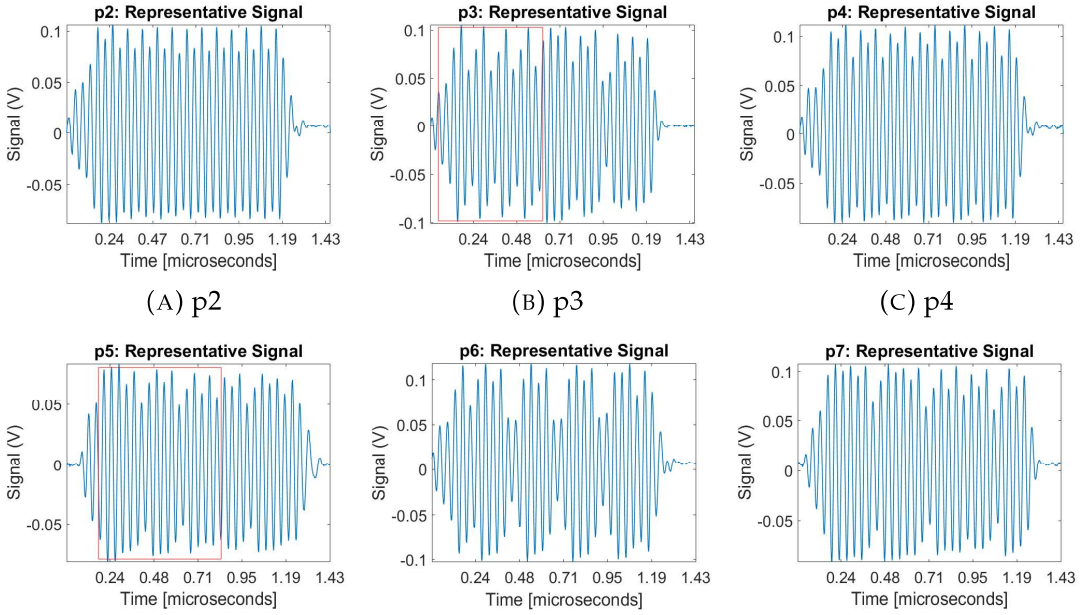

(A) p2 (B) p3 (C) p4

(D) p5 (E) p6 (F) p7

FIGURE 2.7: Representative signals for nonlinear bubble oscillations

all 30 oscillations and thus, bursts. This was also evident in signal power spectra which would have more broadband shapes in comparison to the other signals. These broadband signals were classified as **Burst** and analyzed separately (see figure 2.8 for a time domain representation).

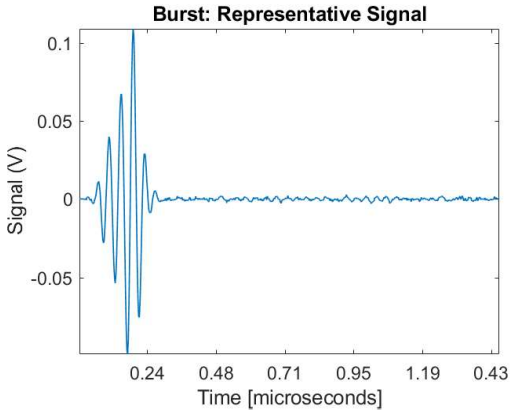

FIGURE 2.8: Representative signal of a bursting bubble.

Once the signals were isolated, the classified signals were examined to

track the total number of signals that are classified into the five groups: (1) linear, (2) linear and increasing in amplitude (growth), (3) linear and decreasing in amplitude (dissolution), (4) nonlinear and (5) burst signals.

2.4 Multimodal Imaging

2.4.1 Experimental Setup

PA and US multimodal imaging was done using the Vevo LAZR 2100 system with LZ250 transducer operating at 21 MHz central frequency (13-24 MHz bandwidth) (figure 2.9). The transducer is a 256-element linear array transducer coupled with a laser ($\lambda = 680 - 970$ nm) system (figure 2.10a). The transducer and laser have a common focus at 11 mm imaging depth.

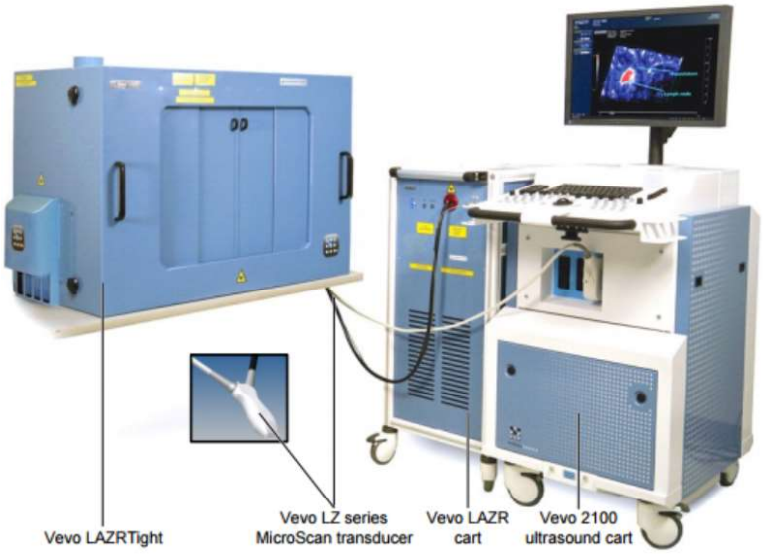

FIGURE 2.9: Vevo LAZR 2100 System

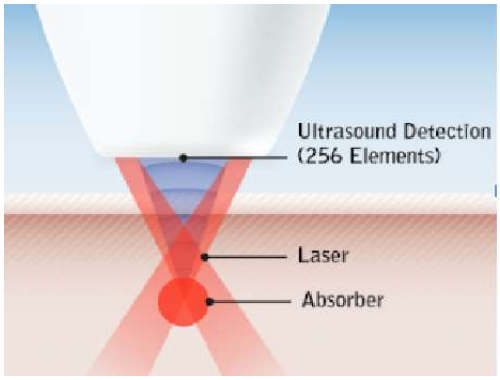

(A) LZ250 Transducer

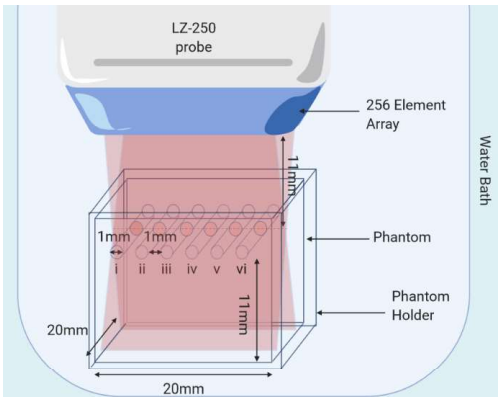

(B) Vevo LAZR- experimental setup

FIGURE 2.10: Vevo LAZR- Multimodal Imaging Setup: (A) LZ 250 Transducer and laser; 21 MHz central frequency (13-24 MHz bandwidth. (B) experimental setup with phantom, trasnducer and laser alignment with respect to vessels for cross-sectional imaging

In multimodal imaging mode on the Vevo LAZR, alternating laser and US pulses are delivered to a fixed ROI.

10%, 10kPa Polyacrylamide phantoms containing six 1mm diameter vessels were prepared the day of imaging using degassed, deionized (DDI) water. The deionized water was degassed using a SRDS-1000 (FUS Instruments, Toronto) water degassing system. For each phantom, the polyacrylamide solution was prepared and poured into a 2 cm by 2 cm holder with six parallel fire-polished borosilicate vessels, each 1 mm in outer diameter. The six borosilicate vessels were carefully removed after polymerization of the polyacrylamide solution and the phantom was removed from the holder for temporary storage. In storage, phantoms were hydrated in PBS in a beaker at room temperature.

Prior to imaging, the vessels were filled with activated solutions of SBNBs each at a 1: in 30 dilution. The phantom was replaced in the phantom holder and the vessels were sealed at the ends using glass slides. The sealed phantom-in-holder

was placed in a DDI water bath for imaging. The center of the vessels were approximately aligned at the laser-transducer focus (see setup schematic in figure B.2).

US and PA RF data were acquired simultaneously when acquiring PA images. US images were collected at 4% transducer power (1.890 MPa) and PA images at 100% laser power at a wavelength of 700 nm. 25 frames of US and PA images were acquired and were subsequently analyzed using MATLAB. The gain for US imaging was set at 35 dB for each measurement and the gain for PA imaging was set to 60 dB for each measurement.

2.4.2 Data Analysis

US/PA data from the six contrast agents were analyzed using Matlab R2019a. The laser energy was recorded for each frame and used to normalize the PA RF-data before further analysis.

To analyze the intensity differences for each vessel, a mask was created of circles with centers corresponding to the centers of the vessels and diameters matching vessel diameter (as determined from the US image). The mask was multiplied by the log-compressed RF-matrix to isolate the signal from each vessel. The average signal from a vessel was determined by taking the mean signal expressed by all pixels within a single vessel region. This was determined and averaged for all 25 frames and all 9 cross sections of the same vessel type. The standard deviation of the mean vessel signal of the 9 cross sections of each vessel was determined. The maximum signal from all pixels within a vessel region was also determined with an average and standard deviation of all 9 cross sections.

To analyze the harmonic content generated by the bubbles within the vessel a square ROI was selected from within each vessel region excluding the boundary regions of vessels. The RF-line was plotted without a log compression. From the RF-line the Fast Fourier Transform was applied and the power spectra of each RF-line from each vessel was averaged for all 25 frames of all 9 cross sections. The normalized power spectra were obtained by dividing the spectra by its corresponding maximum power.

2.5 Statistical Testing

Where applicable, a test of significance was done to identify differences between groups. In statistics, one-way analysis of variance (ANOVA) is a technique that can be used to compare means of two or more samples using the F-distribution. ANOVA tests the null hypothesis, that samples in all groups are drawn from populations with the same mean values. The ANOVA produces a statistic (F-statistic) that represents the ratio of the variance among the means to the variance within the samples. The p-value is the probability that the test statistic can take a value greater than the value of the computed test statistic. A higher F-statistic implies that at least 2 samples were drawn from populations with different mean values. The p-value is used to define statistical significance between the means of populations that exhibit the highest differences. If the results of a one-way ANOVA indicate differences in the means, pairwise comparison results from a multiple comparison, Tukey-Kramer statistical test were used to identify which groups differ from one another.

A one-way ANOVA test using the MATLAB R2019a ®function *anova1()*

was used for an initial assessment of statistical significance of mean differences between formulation types. By convention researchers use a sliding scale (summarized in table 2.4) to classify results from a statistical test where the comparison of the p-value to the test statistic provides information on the level of significance [90]. If a small p-value ($p < 0.05$) was obtained, it was determined that at least two groups exhibit significant differences. In order to identify which groups were different, a multiple comparison of means was performed using the statistics from the one-way ANOVA test and the function *multcompare()* in MATLAB R2019a®.

TABLE 2.4: Statistics Table: Sliding scale of statistical significance

P-value	**Significance Level**
$p < 0.01$	highly significant
$0.01 < p < 0.05$	statistically significant
$0.05 < p < 0.1$	tending toward statistical significance
$0.1 < p$	not statistically significant

Chapter 3

Results and Discussion

3.1 Results

3.1.1 Agent Validation

TEM images of the agents after activation were collected. With a scalebar of 200nm, the representative TEM images of 0 (figure 3.1a), 0.3 mg (figure 3.1b) and 0.5 mg (figure 3.1c) SBNBs are shown. These images present evidence of NBs with $\sim$300 nm diameter. Dark ridges on the bubble surface show what is thought to be shell buckling. Also present in the background of the images are flecks which are attributed to patches of density differences due to the nonbuoyant lipid population.

Using the Archimedes mass resonant measurement system, the average buoyant particle concentration of three measurements is presented for each activated SBNB formulation in figure 3.2a. Bubble yields were consistently orders of magnitude higher than previously developed agents (1×10^{11} as compared to 1×10^{9}). From a one-way ANOVA test to compare the differences between all of the measured concentrations, an F-statistic of 2.9993 and a p-value of 0.0552 was

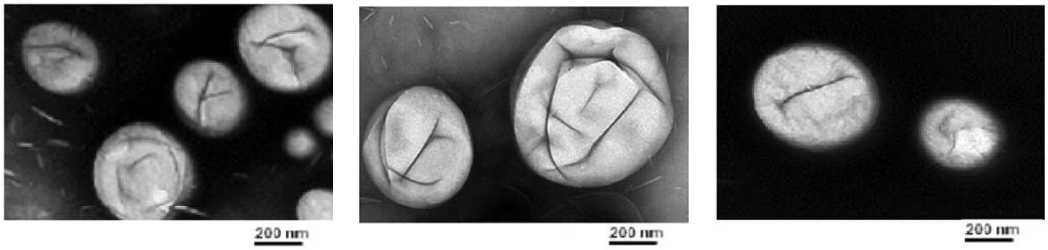

(A) TEM - Undyed Nanobubbles (B) TEM - 0.3 mg Sudan Black Nanobubbles (C) TEM - 0.5 mg Sudan Black Nanobubbles

FIGURE 3.1: Transmission Electron Microscopy images of SBNBs ($scalebar = 200nm$)

obtained indicating that differences between bubble yields for various SBNB formulations are not significant (ns).

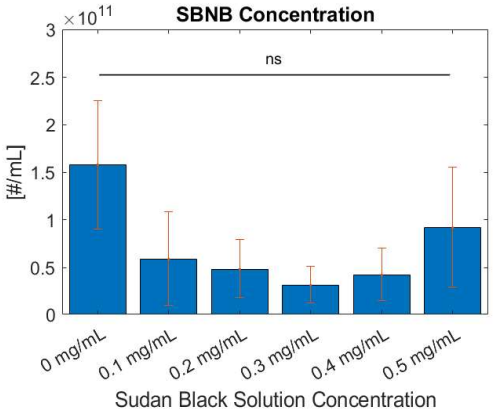

(A) Nanobubble Concentration Comparison ($n = 3$)

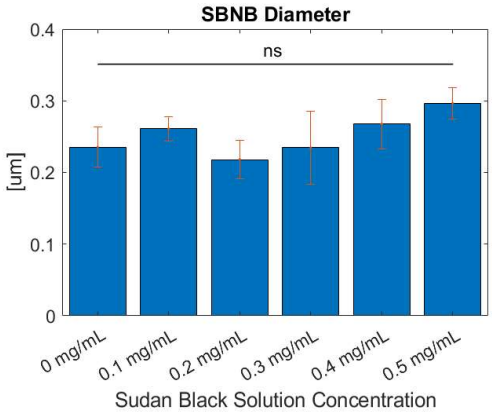

(B) Nanobubble Size Comparison ($n = 3$)

FIGURE 3.2: Resonant Mass Measurement Data - SBNB concentration and diameter

The average buoyant particle diameter is presented comparing each of the 6 formulations (see figure 3.2b). From a one-way ANOVA test, which compares the differences between all the average measured diameters of all formulations, an F-statistic of 2.39 and a p-value of 0.1001 was obtained indicating that differences between the average bubble diameter for varying bubble formulations were not significant.

3.1.2 Surface Tension

From pendant drop tensiometry measurements, the surface tension from a droplet of each lipid formulation was tested 20 times. The results of the tensiometry measurements for surface tension are presented in figure 3.3. Compared to water droplets, there is a reduction in surface tension. A steady increase in surface tension is expressed as a function of SB contribution peaking at 0.4 mg/mL.

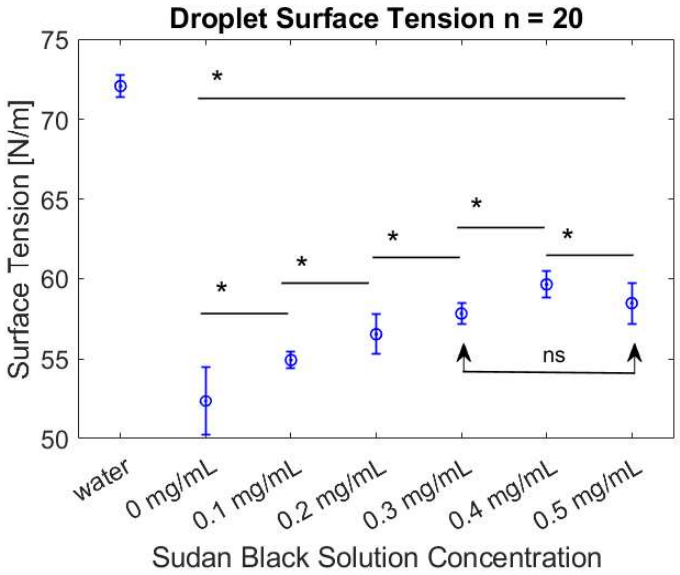

FIGURE 3.3: Surface tension as measured from bulk droplets of lipid solution with varying contribution of SB. Data points are the average of 20 measurements and errorbars represent the standard deviation (* denotes statistical significance; ns denotes no statistical significance). Water was used to show accurate calibration.

From a one-way ANOVA test to compare the differences between the measured tensions, an F-statistic of 93.42 and a p-value of 1.16e-38 was obtained. This indicated statistically significant differences between at least two droplet types. A multiple comparison of the mean surface tension of the droplets was performed to identify groups of significance (summarized in table 3.1). As shown by the horizontal bars in figure 3.3, all lipid formulations with SB dye were determined to be

TABLE 3.1: Lipid-Droplet Surface Tension

SBNB type	**Average Surface Tension** $[N/m^2]$	**Standard Deviation** $[N/m^2]$
0 mg/mL	52.360	$\pm$ 2.114
0.1 mg/mL	54.936	$\pm$ 0.518
0.2 mg/mL	56.542	$\pm$ 1.239
0.3 mg/mL	57.829	$\pm$ 0.635
0.4 mg/mL	59.638	$\pm$ 0.844
0.5 mg/mL	58.471	$\pm$ 1.263

statistically different (*) from the 0 mg/mL formulation. Each formulation type had statistical significance when compared to the formulation with 0.1 mg/mL difference in SB solution concentration. However, the difference between the 0.3 mg/mL lipid and 0.5 mg/mL lipid was determined to be insignificant (ns). Water droplets were not included in the significance tests.

3.1.3 Single Bubble Excitation

The total number of registered signals above threshold from a singular bubble with respect to acoustic pressure is presented in figure 3.4. The classified linear and nonlinear signal counts were compared as a function of SB contribution.

Upon excitation of activated, diluted, and pore-filtered SBNBs, differences were seen between the total number of detected bubbles. This is visible upon comparison of the y-axes in 3.4. SB formulations generated signal counts on the same order of magnitude of each other and approximately half that of the 0 mg/mL formulation, at approximately equal initially concentrations of NBs.

The lowest bubble activity was recorded at the minimum pressure (0.2

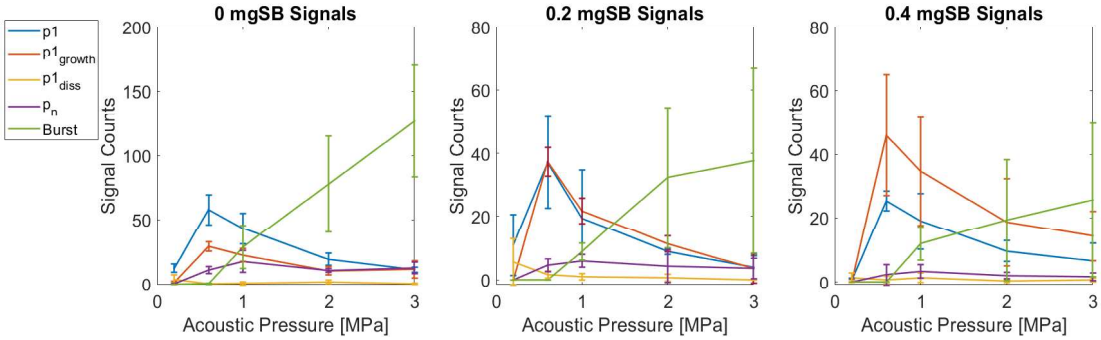

FIGURE 3.4: Single Bubble Signal Count as a function of acoustic pressure ($n = 3$)

MPa) for all three formulations. Here, we use bubble activity to refer to the number of counts registered above threshold. At this low pressure, the 0 mg/mL SBNB formulation generated the most counts. Detected bubble behaviour by all formulations at 0.2 MPa was dominated by $p1$ signals. No nonlinear signals were detected at 0.2 MPa. As the pressure of the incident acoustic wave increased, an increase in the number of linear and nonlinear counts was recorded.

At 0.6 MPa, the number of $p1_{growth}$ and $p1_{diss}$ signals increased. The counts of $p1_{growth}$ signals were recorded maximum at 0.6 MPa and decreased with increasing pressure. This peak at 0.6 MPa was consistent among all three formulations tested. Additionally, as the SB contribution increases, the number of $p1_{growth}$ signals detected increases (red line) and dominates the number of signals detected. Here, more $p1$ signals (blue line) were recorded on average than $p1_{growth}$ signals (red line). In the case of 0.2 mg/mL formulation, $p1$ and $p1_{growth}$ signal counts were approximately equal. The 0.4 mg/mL formulation, however generated counts of $p1_{growth}$ signals that surpassed $p1$ counts. This increase in bubble growth behaviour is an indication that the addition of SB to the bubble lipids increases the tendency for gas exchange across the NB shell.

Beyond 0.6 MPa, counts of linear signals ($p1$, $p1_{growth}$, and $p1_{diss}$) decreased. The maximum number of p1 signal counts occurred at 0.6 MPa, after which the count decreased (blue line). A peak in nonlinear signals occurred at 1 MPa for all NB formulations (purple line). A steady increase in bubble bursting started at 1 MPa and peaked at 3 MPa (green line). No bubble bursts were detected before 1 MPa for any of the NB formulations.

In order to identify the types of signals that most significantly contributed to the total number of signals detected by a particular formulation, the average percent of registered signals above threshold for each signal type was plotted and compared (see summary table in Appendix A). This data is presented in figure 3.5. A test of significance was done to compare the average contributions of each signal type to the total number of registered signals (statistical data provided in Appendix A).

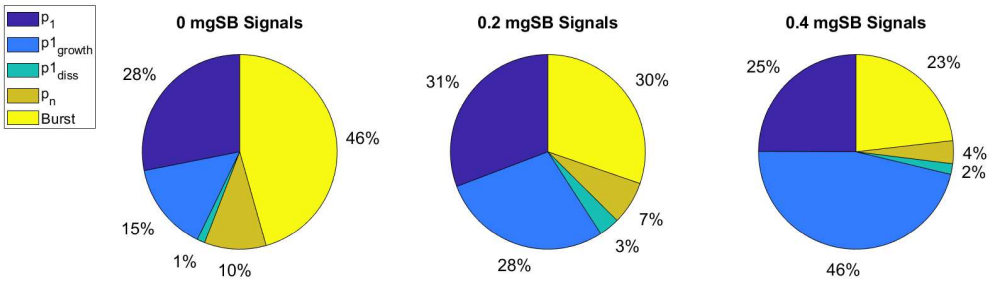

FIGURE 3.5: Average Contribution of signal types to total signal count summed over all pressures ($n = 3$); average total number of signals = 511 (0 mg/mL), 261 (0.2 mg/mL), 246 (0.4 mg/mL)

In figure 3.5, no apparent trend is observed for p_1 signals. However, upon the addition of SB dye,the number of $p1_{growth}$ increases with statistical significance. On average, the $p1_{growth}$ signals contribute approximately twice as much to the total signal count of 0.2 mg/mL SBNBs compared to the NBs without dye. Similarly

the 0.4 mg/mL SBNBs had ∼three times more $p1_{growth}$ signals than the 0 mg/mL NBs. This data further supports the idea that the addition of SB to the bubble lipids increases the tendency for gas exchange across the NB shell. No apparent trend with increasing dye concentration is observed for $p1_{diss}$ oscillations. The number of the various p_n signals were low (see Appendix A). However, the contribution of all p_n signals to the total number of signals detected from the NB formulation decreased with increasing SB concentration tending toward statistical significance ($p < 0.1$). This data is consistent with the idea that the addition of SB to the bubble lipids decreases the nonlinear behaviour of the NBs. Additionally, as observed in figure 3.5, the total contribution of bursting signals decreased as a function of SB. Burst signal counts and total signal counts, however, varied greatly across samples and therefore this trend was not established with statistical significance (see Appendix A).

3.1.4 Multimodal Imaging

Multimodal US/PA images were collected using the Vevo LAZR system. A representative image of the 6 vessels filled with a 29:1 (PBS:SBNBs) dilution as a function of SB is shown in figure 3.6. The top image is the PA image and the bottom image is the corresponding US image collected simultaneously.

The PA image in figure 3.6a shows only 5 clearly identifiable vessel cross sections with increasing PA signal amplitude. The increase in signal corresponds to the increase in dye contribution. As expected, the first vessel, containing undyed NBs generated little detectable signal due to the low absorption profile of lipids. In comparison, in figure 3.6b all 6 vessels are clearly identified in the US image. High

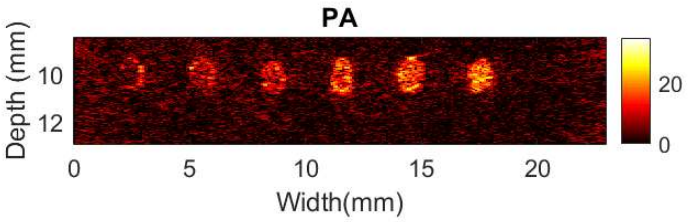

(A)

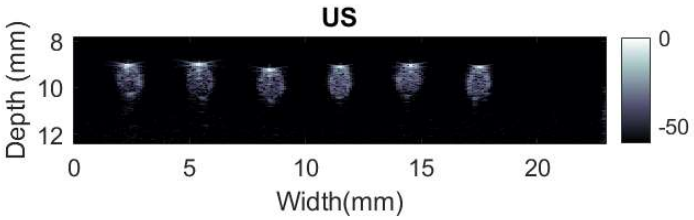

(B)

FIGURE 3.6: Representative US/PA multimodal images with vessels containing 1:29 dilution of 0 mg, 0.1 mg, 0.2 mg, 0.3 mg, 0.4 mg, 0.5 mg Sudan Black from left to right

amplitude signal at the top of each vessel cross section corresponds to differences in acoustic impedance caused by the vessel walls. Within the vessel, US speckle indicates the presence of unresolved scatterers. In contrast to the PA image, the US images featured small differences in backscatter between the bubble populations in the vessels of the figure 3.6b.

An analysis of the average PA and US power is summarized in figure 3.7. An analysis of the the maximum vessel power averaged across all vessel cross sections is summarized in figure3.8. Horizontal lines marked by a star (*) are used to indicate groups that are statistically different from one another, as determined from one-way ANOVA and multiple comparisons tests. Table 3.2 summarizes the F-statistics and p-values obtained from the ANOVA tests describing the significance of the null hypothesis that no mean signal measured was different from another.

Tests that produced a small p-value ($p < 0.05$) were followed by a multiple comparison test. The total number of statistically different groups from each signal measurement was also reported in table 3.2. Pairs with statistical significance are also denoted in each of the summary figures (3.7 and 3.8) by a star. Table summaries of pairwise statistics associated with figures 3.7 and 3.8 are provided in Appendix A.

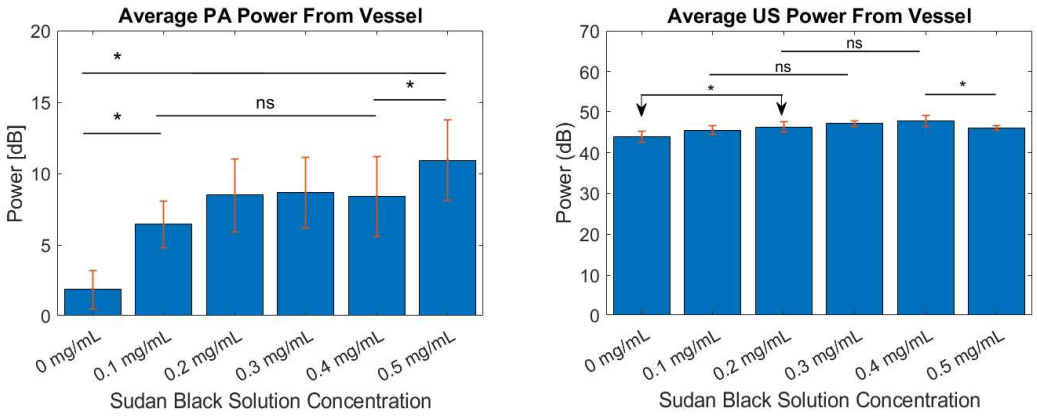

(A) Average PA signal from vessel cross section ($n = 9$)

(B) Average US signal from vessel cross section ($n = 9$)

FIGURE 3.7: Average PA and US signal from SBNBS

The computed average PA power from the vessel cross sections (figure 3.7a) shows that an increase in average PA power occurs with increasing SB solution concentration. This was consistent with the visual in figure 3.6a. The differences between the average PA power of any SB dyed bubbles with the undyed bubble formulation was statistically significant. Additionally, the Average PA Power of the 0.5 mg bubble formulation was also determined to be different from the other NB formulations with statistical significance. The groups with SB dye ranging from 0.1-0.4 mg SB B integration were determined not to be statistically different from one another.

The computed average US power from the vessel cross sections (figure 3.7b) showed a trend of increasing power with increasing SB (visible in figure 3.6b).

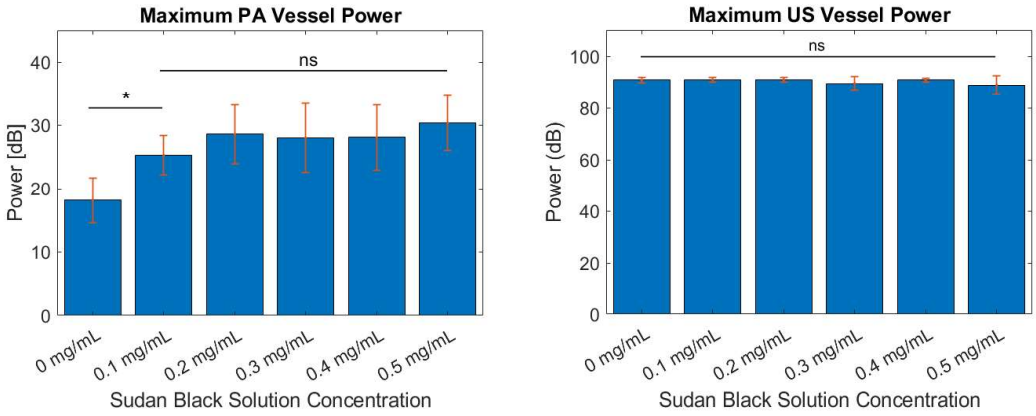

(A) Maximum PA signal from vessel cross section ($n = 9$)

(B) Maximum US signal from vessel cross section ($n = 9$)

FIGURE 3.8: Average PA and US signal from SBNBS

TABLE 3.2: Vevo LAZR Imaging: one-way ANOVA Statistics

Experiment type	**F-statistic**	**P-value**
Average PA	14.54	1.135E-8
Average US	9.11	3.825E-6
Maximum PA	8.01	1.486E-5
Maximum US	1.86	0.118

A test of significance indicated a statistical difference between 0.1, 0.2 an 0.3 mg/mL SBNBs in a pairwise comparison with undyed NBs (see statistical comparison in Appendix A). Statistical difference between the average US power of 0.5 mg SBNBs and 0.4 mg SBNBs was also established. However, the groups with SB dye ranging from 0.1-0.4 mg SB integration were determined not to be statistically significant in difference from one another.

When comparing the average maximum PA power shown in figure 3.8a statistical analysis identified significance between the maximum power generated from undyed bubbles, and any of the SBNB formulations. No significant difference was expressed in maximum PA power between varying formulations with SB. No

significant difference was found between the maximum US power for the various SBNBs.

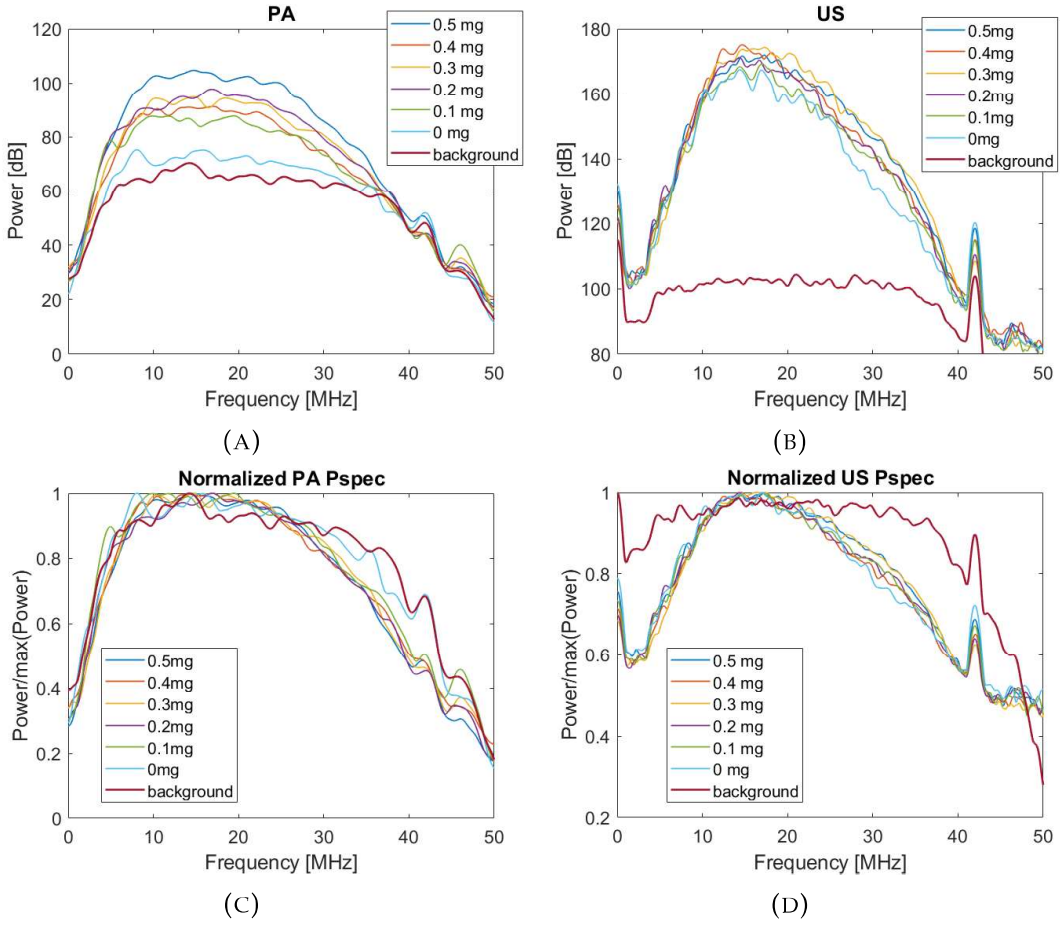

FIGURE 3.9: Average PA and US power spectra from SBNBS

In the frequency domain, the average power spectra of RF-data from within vessel regions were averaged for PA and US, and normalized to their maximum power as presented in figure 3.9.

The PA power spectra (figure 3.9a) are consistent the time-domain data with respect to differences in power from various vessels. The 0.5 mg SBNBs generated the highest peak power in spectra and all vessels produced signal above

the noise floor. When investigating the normalized PA power spectra (figure 3.9c) SBNBs produce a narrower spectra than the 0 mg NBs. No clear difference appears between the various spectra from dyed NBs.

The US power spectra (figure 3.9b) show minimal separation between the various NB types. The SBNBs signals produced overlapping spectra. The 0 mg NBs spectra presents sharper defined features in the form of peaks at $\sim$16 and $\sim$19MHz. The lowest peak power was generated by the 0 mg NBs (light blue line). All SBNBs generated acoustic power over 150 dB above the noise floor (brown line) at the central frequency, indicating a high signal to noise ratio.

3.2 Discussion

3.2.1 Agent Validation

TEM images of the agents in figure 3.1 provide evidence of NB populations. The number of images collected are too few to make a conclusion on the average differences in bubble shape and quality between SBNB types. However, dark ridges on the bubble surface show shell buckling which is thought to play an important role in bubble dynamics [10]. Bubble background in TEM images show populations of nonbuoyant particles visible as flecks. This is most evident in figure 3.1a.

Archimedes testing of SBNB concentration and diameter (figure 3.2) provide no evidence of differences between SBNBs. Despite visible trends in the data, the standard deviation of the populations represented by the errorbars in figure 3.2 are too high. Representative size distribution curves for the various SBNB formulations are provided in appendix A.

3.2.2 Surface Tension

In pendant drop tensiometry, the drop dimensions (figure 2.4) are affected by the incorporation of surfactants. Fitting the drop dimensions to the Young-Laplace equation yields a measure of surface tension. Measured differences in surface tension for the various SB lipid formulations were found to have statistically significant differences. In figure 3.3 from 0 to 0.4 mg/mL a linear trend is evident of increasing surface tension with SB contribution. Upon the lowest addition of SB to

the lipid solution (0.1 mg/mL), a 1% increase in surface tension was measured compared to the control (0 mg/mL). The maximum change in surface tension measured was from the 0.4 mg/mL lipid formulation (13.9% higher than the control). Beyond 0.4 mg, the measured difference in surface tension decreased. This decrease could be an indication of a critical concentration of SB. If so, at concentrations above the critical threshold, further addition of SB may not incorporate into the membrane. A study of SB precipitation may address this question.

For the results presented, surface tension values obtained were measured at the air-lipid interface. Because the SBNBs use a PFC gas core, a more accurate measurement of the NB tension would use a PFC atmosphere. Pendant Bubble Rising Drop methods would usually be able to achieve this by producing gas vesicles inside the lipid solution using a syringe equipped with a J-shaped needle. This setup, however, requires the lipid solution to be transparent and is therefore not a practical setup for the opaque SBNB lipid solution. Evidence has been presented to suggest that the decrease in surface tension for the PFC-lipid interface in comparison to the air-lipid interface is approximately linear [91]. Therefore, the differences in surface tension observed here can be assumed to exhibit the same trend for the PFC-lipid interface. Overall, SB increases the surface tension at the air-lipid interface.

The mechanism behind the higher stability and acoustic backscatter of NB populations in comparison to theoretical predications is thought to be, in part, influenced heavily by the biophysical properties of the bubble-stabilizing shell. The Laplace pressure predicts size-dependent stability of an uncoated NB as a result of pressure differences on either side of the bubble wall. Recently, changes in membrane surface tension at different degrees of compression via optical tensiometry

experiments were shown to correspond to differences in bubble stability [91]. The surface tension measurements presented here may influence the overall stability of SBNBs (see Appendix), however, the effects of SB on NB stability have not been rigorously investigated.

It has been numerically and experimentally established that the gas from a bubble will readily dissolve in water, driven by the undersaturation of dissolved gas in the surrounding aqueous solution and the surface tension of the gas bubble-water interface through a Laplace overpressure in the bubble [92][93]. Surface tension generates a higher pressure inside the bubble and drives the diffusion of gas across the membrane [24]. Therefore, the SB dependent increase in surface tension as established in figure 3.3 contributes to gas transfer across the membrane.

3.2.3 Single Bubble Excitations

Most prevalent in the single bubble experiments is the trend of increasing bubble growth with increasing SB contribution. Our single-bubble excitation findings of shell permeability are in agreement with findings of differences in surface tension and the modelling by Sarkar et al. In that work, added interfacial elasticity resulted in different dissolution dynamics when interpreted through an analytical expression for the dissolution time for an encapsulated air bubble [24]. They showed that increasing the permeability of the shell linearly decreases the dissolution time, and therefore increases the rate of gas exchange across the shell. Dissolution of the SBNBs under Laplace pressure drives the lipid molecules to pack into a tensionless state [24]. It is therefore energetically favourable for shells with

higher surface tension to undergo gas exchange across the shell. Comparing the average slope of the dissolution signals could be an area of future study for measuring comparable shell permeability with new surfactants.

From the Laplace pressure theories on size-dependent agent stability, we would expect the effects of increased shell permeability and rates of dissolution would be more prevalent for NB populations. The disproportionate count of growth signals in comparison to $p1_{diss}$ signals measured in all NB experiments may have several explanations. In the case of a PFC-core bubble investigated by Sarkar et al, a bubble with initial radius of 1 μm would dissolve in 2500 s [24], much longer than the 30 cycle time frame investigated here ($\sim$1.4 μs). Additionally, the integration of SB might increase the thickness of the SBNB shell and consequently increase the thickness of the liquid-air mass transfer boundary. What is referred to as the "shell effect" describes the tendency for larger boundary layer thickness to promote more gas to enter the bubble during expansion than out during the compression phase [94]. This is also known as recitified diffusion. Moreover, if the SB forces a separation of the lipid surfactants, the surface area of the shell would also increase. According to the "area effect", more gas tends to enter the bubble during bubble expansion when the surface area is larger [94]. It is also important to note that the surface area of the NBs can increase as a function of SB without an increase in NB volume if shell buckling also increases.

Single bubble excitations of SBNBs exhibited decrease in nonlinear counts in figures 3.4 and 3.5. The observed decrease in total nonlinear signal counts supports the hypothesis that the presence of SB decreases harmonic behaviour of the NBs, however, a strong conclusion cannot be drawn. Due to the low number of signals registered above threshold that were nonlinear for all NB types, all nonlinear

signals were grouped together. One possible explanation of the observed decrease in nonlinear signals could be that SB increase the elasticity of the bubble shell. This would occur if the SB molecules forced a separation of the lipid molecules. A more robust investigation on the effect of SB on NB nonlinear oscillations would require a greater number of sample measurements. Differences in nonlinearity may have gone undetected due to the low overall detection of nonlinear signals.

The decrease in *Burst* signals indicates that the presence of the SB in the NB shell reduces gas diffusion out from within the NB.

3.2.4 Multimodal Imaging

Multimodal US/PA imaging shows clearly detailed images with well delineated vessels in both, PA and US.

The PA imaging results support the use of SB to increase the absorptive properties of lipid shelled NBs. From the smallest contribution of SB tested there was a 4 dB increase in power in comparison to the control (0 mg/mL). The SBNBs with the largest contribution of SB exhibited PA power that was on average 8 dB higher than control.

On average, undyed agents produce low PA signal. Contrast enhancement from the low-absorbing bubble population is possible. From an optical perspective, the lipid shelled bubbles can locally increase optical scattering interactions [95]. By increasing optical scattering, the local fluence increases and the likelihood of optical absorption increases. This can translate to a higher probability of PA interaction.

For SBNBs the PA signal increased with SB concentration. This increase

was not linear. A plateau in signal is seen in both average and maximum PA signal. No significant difference in PA power was seen between the any formulation within the range 0.1-0.4 mg/mL. However, SB has an absorption spectra that is dependent on it's molecular environment. If the SB absorption spectra shifts as a result of decreased presence of lipid molecules or increased presence of other SB molecules, the absorption at 700 nm may decrease. Alternatively, if a critical SB integration threshold occurs at 0.4 mg, as is suggested by surface tension measurements, the increase in signal beyond 0.4 mg may be caused by unbound or precipitous SB. This can be confirmed by testing further contributions of SB beyond 0.5 mg/mL. Additionally, although there is no evidence of SB-dependent attenuation in the PA images, it is possible that differences in acoustic attenuation of the SBNBs are attenuating the PA signals. Comparing the data with images of an equal volume of a non-buoyant particles may be beneficial to determine the effects of the gas core on PA amplitude of SBNBs.

The maximum US power, as shown in figure 3.8b showed no differences between formulation where the average US signal from SBNBs exhibited an increasing power with SB contribution. The discrepancy between the maximum and average US powers may be a consequence of differences in bubble concentration. Although no statistically significant difference in bubble yield was obtained (figure 3.2a), error bars on concentration data ranged by nearly half the concentration. This deviation in concentration can have meaningful consequences on backscatter amplitude because of potentially doubling or halving the gas volume within the ROI.

In the PA frequency domain, the power spectra from the 0 mg/mL NBs most closely resembles the power spectra from a noise region in both, normalized and non-normalized power spectra (figure 3.9). The NB with SB exhibited average

power spectra with minimal differences from each other within the range of the transducer bandwidth (13-24 MHz).

The trend of maximum powers in the US power spectra are consistent with the average vessel signal. Similar to the results in our motivating data (figure 1.6), undyed bubbles display a lower maximum signal than SBNBs. Undyed bubbles present a narrower power spectrum than SBNBs. Within the range of the transducer bandwidth (13-24 MHz) the 0 mg formulation also features the most distinct peaks. When comparing the normalized US power spectra (figure 3.9d) the differences in the spectral features compress suggesting that differences in spectral features are not significant.

Chapter 4

Conclusions and Future Work

4.1 Conclusions

SB dyed NBs were consistently produced with high efficiency. The surface tension of the bulk lipid material was measured. The results show that integration of SB dye into the NB lipid solution increases the surface tension of the bulk shell material. SBNBs were tested under various US conditions. For a single-bubble excitation, it was established that the integration of SB dye into the lipid-shell of a NB increases the growth behaviour of NBs in response to US stimulation. Trends of decreasing nonlinear bubble signal counts, and bubble destruction counts were also detected, however, with low statistical significance. For a population of bubbles under US excitation, the presence of SB produced minimal differences in US signals with some enhanced amplitude compared to undyed bubble populations. This may have been a result in differences in bubble concentration which were not adequately controlled. Bubbles with SB incorporated in the shell also produced broader US power spectra. Finally, analysis of PA and US multimodal images support the use of SB dyed NBs for use in simultaneous US and PA multimodal imaging with SB

dependent PA amplitude. Results show simultaneous enhancement in contrast for both US and PA imaging, where PA enhancement was SB concentration dependent and US enhancement was not.

We conclude that the integration of Sudan Black B in the lipid-shell decreases the nonlinear response nanobubbles. The addition of Sudan Black B also increases rectified diffusion experienced by the agent in response to ultrasound. These differences in bubble dynamics are attributed to physical changes to the shell, namely an increase in surface tension and enhanced shell permeability.

The presence of additional components in a NB shell can have an effect on the amplitude and power spectra of the US signal emitted by the bubble. Understanding how isolated and grouped NBs behave when changes are made to shell composition is vital to the optimal use of NB formulations for US and PA multimodal imaging.

4.2 Future Work

The results show that integration of SB dye into the NB lipid solution increases the surface tension which may play an important role in the stability of SBNBs. Stability of SBNBs at rest, and in response to a stimulant can have important consequences on the feasibility of clinical implementation. Ultrasound contrast agents must be sufficiently stable for storage, handling, injection, and in vivo performance. This study did not address the stability of the various SBNB types. Future work should include a comparison of the stability of unperturbed SBNBs, of SBNBs with repeated exposure to US and with prolonged exposure to PA stimulation.

While the linear bubble behaviour showed significant and reproducible differences in the growth signal counts, no conclusions were drawn from differences in nonlinear bubble behaviour. A more robust study on the nonlinear behaviour with a larger sample size may detect differences.

For a population of bubbles, the presence of SB produced differences in average US power with statistical significance. It is difficult to attribute differences in US power to SB presences due to large fluctuations (almost 3 times) in NB concentration. Microfluidic methods may offer a solution for tighter control of bubble concentration for the comparison of populations of NBs.

While experimental studies are valuable, a theoretical investigation on SBNB dynamics can help identify parameter regions for enhanced bubble activity. The differences in surface tension established in this study can be used in existing bubble models [96] to predict the parameter regions of bubble response [18].

While the main focus of this study was to investigate the effects of Sudan Black B on nonlinear US signal enhancement, further optimization can be done to better tune SBNB use in PA. SB dye experiences a shift in peak optical absorption depending on it's solvent. Therefore, current reports on the peak absorption of SB may be inaccurate. A study of the absorption spectra of SB lipid solutions through spectrophotometry can address this gap and help with closer optimization of SBNBs in the context of PA imaging.

In summary, the next steps should be:

1. to test the stability of unperturbed SBNBs, in response to prolonged US stimulation and to prolonged PA stimulation

2. to repeat single bubble excitations with a specific focus on the nonlinear signals

3. to produce SBNBs with a more finely controlled NB concentration

4. to numerically model NB dynamics to test for predictability of results

5. to measure the optical absorption spectra of Sudan Black B integrated lipid solution

Looking further into the future, clinical applications of SBNBs should be investigated. For instance, in vivo studies can be used to identify the maximum penetration depth of the imaging modalities when SBNBs are employed. MBs are currently in clinical use as ultrasound contrast agents and under active investigation as mediators of therapy. SB bubbles can be engineered in various sizes as vehicles for gas and drug delivery applications. In tumors, hypoxic regions have shown more resistance to chemotherapy, radiotherapy, and photodynamic therapies. Both MBs and NBs have been used for oxygen delivery [97] and have been shown to reverse hypoxic conditions. Potentially, SBNBs can be used as agents with either acoustic or optical triggering beyond the vasculature as theranostic agents for multimodal, targeted oxygen delivery.

Appendix A

Supporting Data

A.1 Shell Membrane Constituents

The components of the shell membrane are presented below in table A.1. The molecular weight and total molar contribution per 1 mL (or per vial) is summarized. For ease in interpretation and better understanding of the contribution of each component to the total shell constitution that ratio of each component is normalized to DSPE-mPEG 2k.

TABLE A.1: Shell Membrane Constituents; light grey: surfactants; dark grey: co-surfactants; green: additives

Components	Molecular Weight	Mass per 1 mL solution (mg)	mmoles	Ratio
DSPE-mPEG 2k	2805.5	1.0	3.56E-4	1
DPPA	670.9	1.0	1.49E-3	4
DPPE	692.0	2.0	2.89E-3	8
DBPC	902.4	6.1	6.76E-3	19
Glycerol	92.1	126.0	1.37	3838
Propylene Glycol	76.0	104.0	1.37	3839
Sudan Black B	456.5	2.19E-4-10.95E-4	0.1-0.5	0.6-3.1

A.2 Bubble Size Distribution Curves

This appendix contains the graphs which show the size distribution for the experiments done in this work. The SBNB size distribution graphs were acquired from measurements done using Archimedes (Malvern Panalytical, MA, USA). The Archimedes system measures both buoyant (bubbles) and non-buoyant particles (micelles) which are both included in the graphs. The average diameter and estimated bubble concentration is also measured by the Archimedes system and is included for each NB formulation.

A.2.1 Unfiltered Measurements

Bubbles were activated through mechanical agitation using a Vialmix (Bristol Myers Squibb(BMS), NY, USA) mechanical shaker. NBs were isolated through

differential centrifugation. Drawing from the inverted vial limited mixing of activated bubbles and help control for bubble size distribution. Without further filtration, these samples were diluted (1:500 dilution) and measured for size distribution and concentration. Representative size distribution curves are shown in figure A.1.

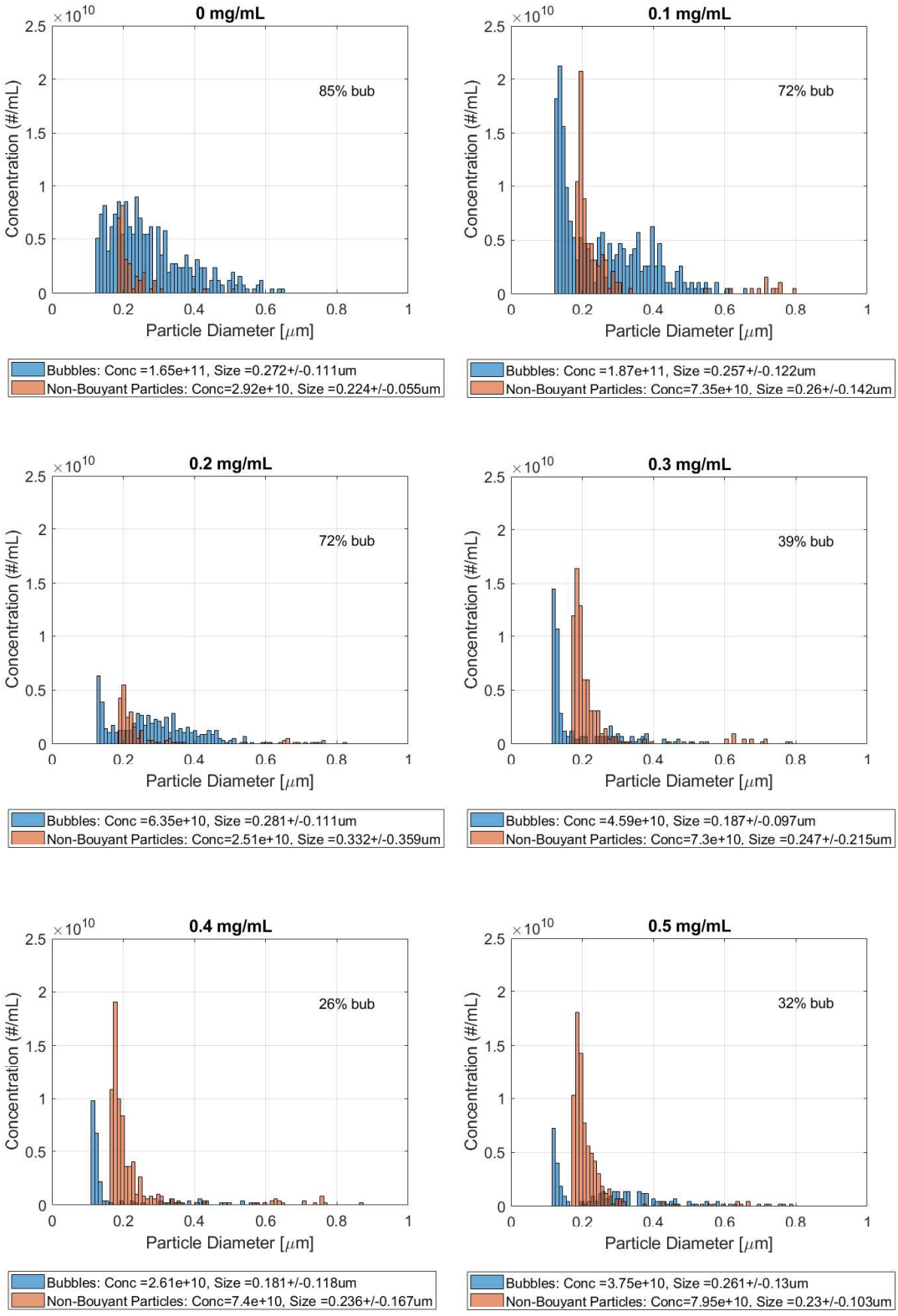

FIGURE A.1: Representative size distribution curves for SBNBs

Without filtration, activated SBNBs were measured on the range of 100-900 nm. A subpopulation of non-buoyant particles likely in the form of mycelles or lipid sheets was also present. No registered counts occur at 100 nm or below as 100nm is the cutoff range for Archimedes sizing on the nanoscale.

A.2.2 Pore-Filtered Measurements

After differential centrifugation SBNBs were diluted (1:10 in PBS) and filtered using 450 nm pore size. These samples were then measured for size distribution and concentration. Because filtered populations were only used for the single bubble experiments, only the 0 mg, 0.2 mg and 0.4 mg/mL SBNBs were filtered and sized. Representative size distribution curves are shown in figure A.2. The concentration data presented was corrected for dilution before plotting.

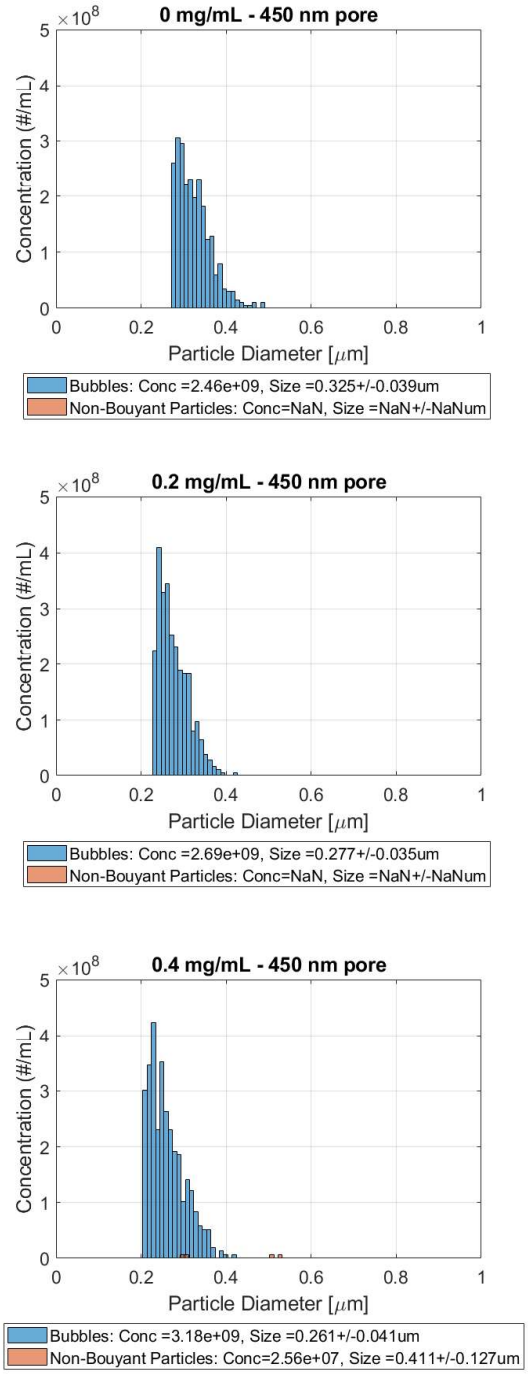

FIGURE A.2: Representative size distribution curves for pore-filtered SBNBs

Filtration using a 450 nm pore size filter successfully limited all SBNB populations below the 450 nm threshold as seen in figureA.2. The process of filtration is destructive in nature and therefore significantly decreases the SBNB yield (From $\sim 1 \times 10^{11}$ to $\sim 1 \times 10^{8}$). The reduced concentration of SBNBs, however, is still comparable to that of previously produced agents. The non-buoyant particle population was significantly reduced.

A.3 Summary Statistics: Pairwise Values

Please note: for the following pairwise comparisons * indicates ($p < 0.1$) and ** indicates ($p < 0.05$).

A.3.1 Surface Tension

TABLE A.2: Statistics Table: Surface Tension (n = 20)

Reference Sample	**Pair Sample**	**p-value**
0 mg/mL	0.1 mg/mL	3.40E-8**
0 mg/mL	0.2 mg/mL	2.07E-8**
0 mg/mL	0.3 mg/mL	2.07E-8**
0 mg/mL	0.4 mg/mL	2.07E-8**
0 mg/mL	0.5 mg/mL	2.07E-8**
0.1 mg/mL	0.2 mg/mL	8.94E-4**
0.1 mg/mL	0.3 mg/mL	2.09E-8**
0.1 mg/mL	0.4 mg/mL	2.07E-8**
0.1 mg/mL	0.5 mg/mL	2.07E-8**
0.2 mg/mL	0.3 mg/mL	0.015**
0.2 mg/mL	0.4 mg/mL	2.07E-8**
0.2 mg/mL	0.5 mg/mL	3.25E-5**
0.3 mg/mL	0.4 mg/mL	1.18E-4**
0.3 mg/mL	0.5 mg/mL	0.56
0.4 mg/mL	0.5 mg/mL	0.036**

A.3.2 Bubble Population: US and PA

TABLE A.3: Statistics Table: Average PA Power (n = 6)

Reference Sample	**Pair Sample**	**p-value**
0 mg/mL	0.1 mg/mL	0.0029**
0 mg/mL	0.2 mg/mL	8.10E-6**
0 mg/mL	0.3 mg/mL	4.62E-6**
0 mg/mL	0.4 mg/mL	1.08E-5**
0 mg/mL	0.5 mg/mL	2.51E-8**
0.1 mg/mL	0.2 mg/mL	0.4902
0.1 mg/mL	0.3 mg/mL	0.3924
0.1 mg/mL	0.4 mg/mL	0.5428
0.1 mg/mL	0.5 mg/mL	0.0036**
0.2 mg/mL	0.3 mg/mL	1.0000
0.2 mg/mL	0.4 mg/mL	1.0000
0.2 mg/mL	0.5 mg/mL	0.2836
0.3 mg/mL	0.4 mg/mL	0.9999
0.3 mg/mL	0.5 mg/mL	0.3681
0.4 mg/mL	0.5 mg/mL	0.2453

TABLE A.4: Statistics Table: Average US Power (n = 6)

Reference Sample	**Pair Sample**	**p-value**
0 mg/mL	0.1 mg/mL	0.3562
0 mg/mL	0.2 mg/mL	0.0155**
0 mg/mL	0.3 mg/mL	2.09E-4**
0 mg/mL	0.4 mg/mL	2.97E-6**
0 mg/mL	0.5 mg/mL	0.0993*
0.1 mg/mL	0.2 mg/mL	0.7182
0.1 mg/mL	0.3 mg/mL	0.0724*
0.1 mg/mL	0.4 mg/mL	0.0024**
0.1 mg/mL	0.5 mg/mL	0.9841
0.2 mg/mL	0.3 mg/mL	0.7275
0.2 mg/mL	0.4 mg/mL	0.1066
0.2 mg/mL	0.5 mg/mL	0.9755
0.3 mg/mL	0.4 mg/mL	0.8130
0.3 mg/mL	0.5 mg/mL	0.2845
0.4 mg/mL	0.5 mg/mL	0.0169**

TABLE A.5: Statistics Table: Maximum PA Power (n = 6)

Reference Sample	**Pair Sample**	**p-value**
0 mg/mL	0.1 mg/mL	0.0223**
0 mg/mL	0.2 mg/mL	2.25E-4**
0 mg/mL	0.3 mg/mL	5.38E-4**
0 mg/mL	0.4 mg/mL	4.86E-4**
0 mg/mL	0.5 mg/mL	1.47E-5**
0.1 mg/mL	0.2 mg/mL	0.6581
0.1 mg/mL	0.3 mg/mL	0.8120
0.1 mg/mL	0.4 mg/mL	0.7956
0.1 mg/mL	0.5 mg/mL	0.2078
0.2 mg/mL	0.3 mg/mL	0.9998
0.2 mg/mL	0.4 mg/mL	0.9999
0.2 mg/mL	0.5 mg/mL	0.9655
0.3 mg/mL	0.4 mg/mL	1.0000
0.3 mg/mL	0.5 mg/mL	0.8907
0.4 mg/mL	0.5 mg/mL	0.9024

A.4 Single Bubble US

A.4.1 Statistics

TABLE A.6: Statistics Table: Mean and Standard deviations for signal contribution (n = 3)

Signal Group	**0 mgSB**	**0.2 mgSB**	**0.4 mgSB**
p_1	28 ± 2 %	31 ± 16 %	25 ± 7 %
$p1_{growth}$	15 ± 2 %	28 ± 2 %	46 ± 19 %
$p1_{diss}$	1 ± 1 %	3 ± 4 %	2 ± 1 %
p_n	10 ± 3 %	7 ± 3 %	4 ± 1 %
$Burst$	45 ± 17 %	30 ± 20 %	23 ± 15 %

TABLE A.7: Statistics Table: ANOVA of mean signal contributions (n = 3)

Signal Group	**F-statistic**	**p-value**
p_1	0.26	0.78
$p1_{growth}$	5.94	0.04**
$p1_{diss}$	0.65	0.55
p_n	4.02	0.08*
$Burst$	1.27	0.35

TABLE A.8: Statistics Table: $p1_{growth}$ signals (n = 3)

Reference Sample	**Pair Sample**	**p-value**
0 mg/mL	0.2 mg/mL	0.36
0 mg/mL	0.4 mg/mL	0.03**
0.2 mg/mL	0.4 mg/mL	0.20

TABLE A.9: Statistics Table: p_n signals (n = 3)

Reference Sample	**Pair Sample**	**p-value**
0 mg/mL	0.2 mg/mL	0.42
0 mg/mL	0.4 mg/mL	0.07*
0.2 mg/mL	0.4 mg/mL	0.37

TABLE A.10: Statistics Table: *Burst* signals (n = 3)

Reference Sample	**Pair Sample**	**p-value**
0 mg/mL	0.2 mg/mL	0.57
0 mg/mL	0.4 mg/mL	0.33
0.2 mg/mL	0.4 mg/mL	0.88

A.4.2 Nonlinear Signal Counts

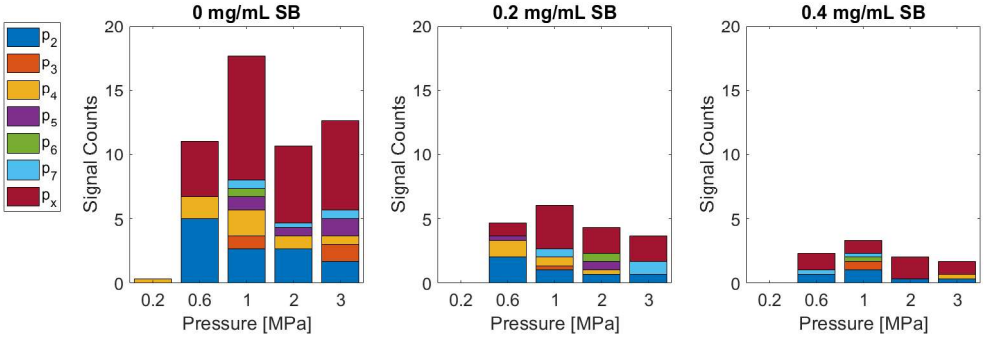

FIGURE A.3: Pressure and dye dependent nonlinear signal counts

Appendix B

Additional Studies

B.1 Testing Stability

In order to characterize the long-term bubble echogenicity, grayscale intensity changes generated by the SBNBs were measured in vitro using a linear transducer (Toshiba, Tochigi-Ken, Japan) and a clinical ultrasound scanner (Toshiba Aplio) at 6 MHz transmit frequency, 12 MHz receiving frequency and a peak negative pressure of 240kPa (mechanical index, 0.1).

Phantoms were custom-designed from agarose mold (1% agarose, 99% H2O). Each phantom had three narrow channels (see figure B.2). Bubbles were stimulated by ultrasound for 8 consecutive minutes. The phantom channels were aligned to the center of the transducer element placed atop such that the transducer was in an inverted orientation.

Activated bubble solution was prepared at constant dilution of stock solution (1 in 100). Six images of each sample were acquired. A ROI was selected within each channel region. The average ultrasound power of all non-zero elements in a

FIGURE B.1: Inverse Bubble Stability Setup

selected ROI was tracked with respect to time for the duration of the 8 min excitation. This data was averaged for all 6 measurements and normalized to data from a noise region within the image. The averaged, normalized power curve for all six measurements is provided in figure B.2a.

Bubble bursting occurs as NB solutions are subject to prolonged US stimulation. The number of bubbles remaining is dependent on the number of bubbles available, as is the case with exponential decay models. As the bubble population decays from bursting, the detected US power should decrease. Under the same conditions, bubble fragmentation and rejoining can occur, and would result in an

increase in US power. This acts as a competing process of bubble bursting and may increase as the average kinetic energy of the stimulated bubbles increases with time due to acoustic radiation force applied by the transducer. If the bubbles expand by absorbing gas from surroundings, as was presented in $p1_{g}rowth$ signals, the US power should also increase.

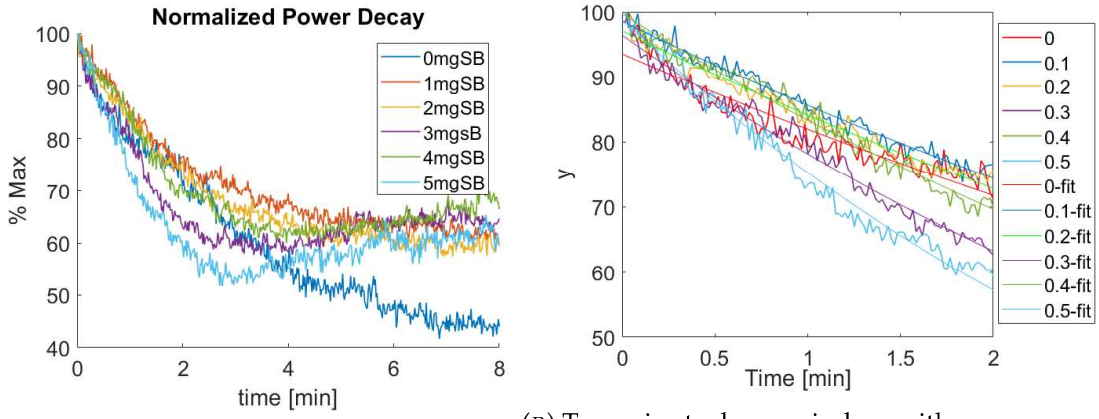

(A) Normalized Power Decay Curve

(B) Two minute decay window with exponential fitting

FIGURE B.2: Ultrasound Stability: Continuous NB Stimulation

In figure B.2a the power decay curve shows a decrease in % maximum US power with respect to time until 2 minutes is reached. After the ∼2 minute time point, the 0.3, 0.4, and 0.5 mg SBNB power curves increase. It is possible that this increase is a result of bubble growth and bubble joining. If only the first 2 minutes of the decay curve are considered, an exponential fit can be used to determine the rate of the population decay in that window. Exponential fits to un-averaged curves were determined (see figure B.2b) to obtain decay rates for the first 2 minutes. These decay rates were obtained for all six measurements and subsequently averaged. Figure B.3 summarizes a comparison of the bubble decay rates for each SBNB formulation. With increasing Sudan Black B contribution an increase in power decay rate is expressed.

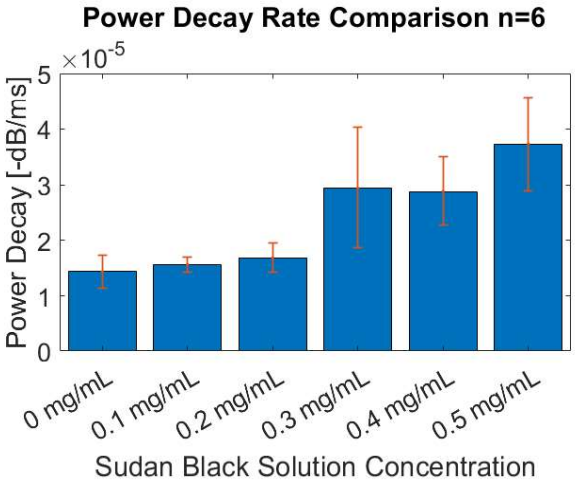

FIGURE B.3: Bubble Decay Rates

This data suggests that an increase in Sudan Black B integration in lipid shell material destabilizes the SBNB formulations. This could be explained by the observed increase in surface tension presented in figure 3.3.

The increase in signal after the 2 minute time point requires further investigation. This phenomenon could be explained by the increase bubble growth signals as established in previous sections. This may further explain the difference in slope after the 2 minute time point between SBNB power curves.

B.2 Bulk Viscosity

To determine the effects of Sudan black on lipid solution viscosity, shear-dependent changes in viscosity were measured using a Thermo Scientific HAAKE MARS III Rheometer at 22 °C using a shear rate sweep. Shear rates were increased linearly from 10 to 100 Hz over 30 s. A total of 100 viscosity points were collected over each shear sweep. These recorded values were averaged for each sample run

for and repeated twice for each NB lipid formulation.

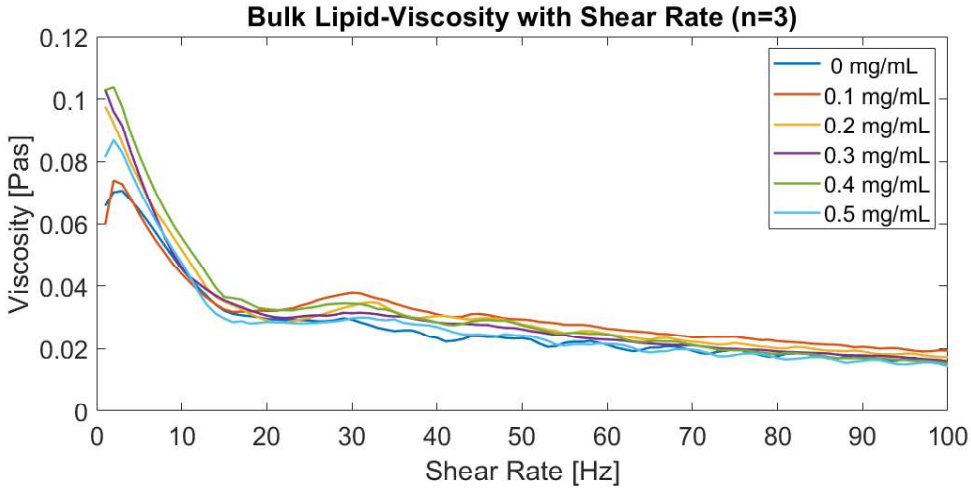

FIGURE B.4: Bulk Lipid Viscosity as a function of shear rate and SB concentration; (n=3)

From figure B.5, no measurable trend is evident comparing SB-lipid formulations as a function of SB concentration or shear rate. The largest variation in viscosity was measured at low shear rates (< 10 Hz). For further investigation, the lowest available rate setting was used in order to test differences at a fixed rate.

The fixed-viscosity was measured at a shear rate of 10 Hz (lowest available setting) at 22 °C for a duration of 30 s. These recorded values were averaged for each sample run for an n = 2 for each NB lipid formulation (see figure B.5).

Figure B.5 presents a moderate trend of decrease in bulk viscosity upon any addition of Sudan Black B dye. With a sample size of 2, however, along with a large variation in standard deviations (indicated by error bars) the data is inconclusive. More measurements for an increased sample size is needed to establish significance and reproducibility.

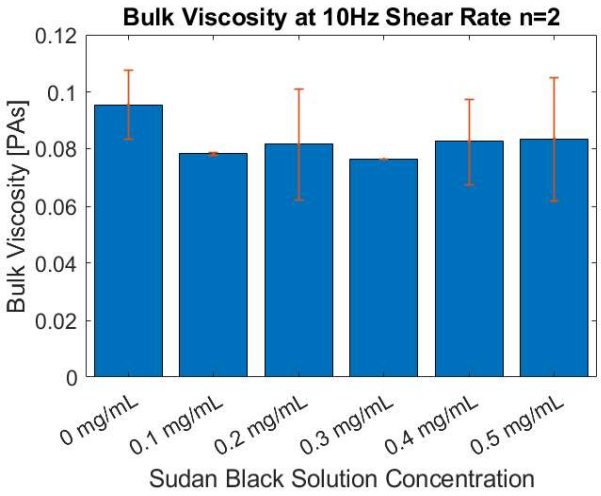

FIGURE B.5: Bulk Lipid Viscosity

Bibliography

[1] P. Beard, "Biomedical photoacoustic imaging", *Interface Focus*, vol. 1, no. 4, pp. 602–631, Jun. 2011. DOI: 10.1098/rsfs.2011.0028. [Online]. Available: https://doi.org/10.1098%2Frsfs.2011.0028.

[2] K. E. Wilson, T. Y. Wang, and J. K. Willmann, "Acoustic and photoacoustic molecular imaging of cancer", *Journal of Nuclear Medicine*, vol. 54, no. 11, pp. 1851–1854, Nov. 2013. DOI: 10.2967/jnumed.112.115568. [Online]. Available: https://doi.org/10.2967%2Fjnumed.112.115568.

[3] C. Kim, R. Qin, J. S. Xu, L. V. Wang, and R. Xu, "Multifunctional microbubbles and nanobubbles for photoacoustic and ultrasound imaging", *Journal of Biomedical Optics*, vol. 15, no. 1, p. 010 510, 2010. DOI: 10.1117/1.3302808. [Online]. Available: https://doi.org/10.1117/1.3302808.

[4] J Zagzebski, "Essentials of ultrasound physics / j.a. zagzebski.", Dec. 2017.

[5] K. K. Shung, "High frequency ultrasonic imaging", *Journal of Medical Ultrasound*, vol. 17, no. 1, pp. 25–30, 2009. DOI: 10.1016/s0929-6441(09)60012-6. [Online]. Available: https://doi.org/10.1016/s0929-6441(09)60012-6.

[6] K. Shung, J. Cannata, Q. Zhou, and J. Lee, "High frequency ultrasound: A new frontier for ultrasound", in *2009 Annual International Conference of the IEEE Engineering in Medicine and Biology Society*, IEEE, Sep. 2009. DOI: 10.1109/iembs.2009.5333463. [Online]. Available: https://doi.org/10.1109/iembs.2009.5333463.

[7] *Diagnostic Ultrasound Imaging: Inside Out*. Elsevier Science & Technology, 2004.

[8] R. H. Perera, C. Hernandez, H. Zhou, P. Kota, A. Burke, and A. A. Exner, "Ultrasound imaging beyond the vasculature with new generation contrast agents", *Wiley Interdisciplinary Reviews: Nanomedicine and Nanobiotechnology*, vol. 7, no. 4, pp. 593–608, Jan. 2015. DOI: 10.1002/wnan.1326. [Online]. Available: https://doi.org/10.1002/wnan.1326.

[9] M. Emmer, A. van Wamel, D. E. Goertz, and N. de Jong, "The onset of microbubble vibration", *Ultrasound in Medicine & Biology*, vol. 33, no. 6, pp. 941–949, Jun. 2007. DOI: 10.1016/j.ultrasmedbio.2006.11.004. [Online]. Available: https://doi.org/10.1016/j.ultrasmedbio.2006.11.004.

[10] N. de Jong, M. Emmer, A. van Wamel, and M. Versluis, "Ultrasonic characterization of ultrasound contrast agents", *Medical & Biological Engineering & Computing*, vol. 47, no. 8, pp. 861–873, May 2009. DOI: 10.1007/s11517-009-0497-1. [Online]. Available: https://doi.org/10.1007/s11517-009-0497-1.

[11] N. de Jong, A. Bouakaz, and P. Frinking, "Basic acoustic properties of microbubbles", *Echocardiography*, vol. 19, no. 3, pp. 229–240, Apr. 2002. DOI: 10.1046/j.1540-8175.2002.00229.x. [Online]. Available: https://doi.org/10.1046/j.1540-8175.2002.00229.x.

[12] S. R. Sirsi and M. A. Borden, "Microbubble compositions, properties and biomedical applications", *Bubble Science, Engineering & Technology*, vol. 1, no. 1-2, pp. 3–17, Nov. 2009. DOI: 10.1179/175889709x446507. [Online]. Available: https://doi.org/10.1179/175889709x446507.

[13] G. Fishbein, "Non-linear acoustic characterization of microbubbles and nanobubbles", Master's thesis, Ryerson University, 2019.

[14] K. Ferrara, R. Pollard, and M. Borden, "Ultrasound microbubble contrast agents: Fundamentals and application to gene and drug delivery", *Annual Review of Biomedical Engineering*, vol. 9, no. 1, pp. 415–447, Aug. 2007. DOI: 10.1146/annurev.bioeng.8.061505.095852. [Online]. Available: https://doi.org/10.1146/annurev.bioeng.8.061505.095852.

[15] S. Qin, C. F. Caskey, and K. W. Ferrara, "Ultrasound contrast microbubbles in imaging and therapy: Physical principles and engineering", *Physics in Medicine and Biology*, vol. 54, no. 6, R27–R57, Feb. 2009. DOI: 10.1088/0031-9155/54/6/r01. [Online]. Available: https://doi.org/10.1088/0031-9155/54/6/r01.

[16] A. J. Sojahrood, E. Stride, R. Karshafian, and M. C. Kolios, "Nonlinear dynamics of polymer shell ultrasound contrast agents at 8-32 mhz ultrasonic excitations", in *2013 IEEE International Ultrasonics Symposium (IUS)*, IEEE, Jul. 2013. DOI: 10.1109/ultsym.2013.0081. [Online]. Available: https://doi.org/10.1109/ultsym.2013.0081.

[17] A. J. Sojahrood and M. C. Kolios, "Classification of the nonlinear dynamics and bifurcation structure of ultrasound contrast agents excited at higher multiples of their resonance frequency", *Physics Letters A*, vol. 376, no. 33, pp. 2222–2229, Jul. 2012. DOI: 10.1016/j.physleta.2012.05.045. [Online]. Available: https://doi.org/10.1016/j.physleta.2012.05.045.

[18] A. Sojahrood, D. Wegierak, H. Haghi, R. Karshfian, and M. C. Kolios, "A simple method to analyze the super-harmonic and ultra-harmonic behavior of the acoustically excited bubble oscillator", *Ultrasonics Sonochemistry*, vol. 54, pp. 99–109, Jun. 2019. DOI: 10.1016/j.ultsonch.2019.02.010. [Online]. Available: https://doi.org/10.1016/j.ultsonch.2019.02.010.

[19] A. A. Doinikov, J. F. Haac, and P. A. Dayton, "Resonance frequencies of lipid-shelled microbubbles in the regime of nonlinear oscillations", *Ultrasonics*, vol. 49, no. 2, pp. 263–268, Feb. 2009. DOI: 10.1016/j.ultras.2008.09.006. [Online]. Available: https://doi.org/10.1016/j.ultras.2008.09.006.

[20] L. J. M. Juffermans, A. van Wamel, R. H. Henning, K. Kooiman, M. Emmer, N. de Jong, W. H. van Gilst, R. Musters, W. J. Paulus, A. C. van Rossum, L. E. Deelman, and O. Kamp, "Ultrasound and microbubble-targeted delivery of therapeutic compounds", *Netherlands Heart Journal*, vol. 17, no. 2, pp. 82–86,

Feb. 2009. DOI: 10.1007/bf03086223. [Online]. Available: https://doi.org/10.1007/bf03086223.

[21] C. Wang, B. Rallabandi, and S. Hilgenfeldt, "Frequency dependence and frequency control of microbubble streaming flows", *Physics of Fluids*, vol. 25, no. 2, p. 022 002, Feb. 2013. DOI: 10.1063/1.4790803. [Online]. Available: https://doi.org/10.1063/1.4790803.

[22] J. E. Chomas, P. Dayton, D. May, and K. Ferrara, "Threshold of fragmentation for ultrasonic contrast agents", *Journal of Biomedical Optics*, vol. 6, no. 2, p. 141, 2001. DOI: 10.1117/1.1352752. [Online]. Available: https://doi.org/10.1117/1.1352752.

[23] G. R. Torr, "The acoustic radiation force", *American Journal of Physics*, vol. 52, no. 5, pp. 402–408, May 1984. DOI: 10.1119/1.13625. [Online]. Available: https://doi.org/10.1119/1.13625.

[24] K. Sarkar, A. Katiyar, and P. Jain, "Growth and dissolution of an encapsulated contrast microbubble: Effects of encapsulation permeability", *Ultrasound in Medicine & Biology*, vol. 35, no. 8, pp. 1385–1396, Aug. 2009. DOI: 10.1016/j.ultrasmedbio.2009.04.010. [Online]. Available: https://doi.org/10.1016/j.ultrasmedbio.2009.04.010.

[25] M. A. Borden and M. L. Longo, "Dissolution behavior of lipid monolayer-coated, air-filled microbubbles: Effect of lipid hydrophobic chain length", *Langmuir*, vol. 18, no. 24, pp. 9225–9233, Nov. 2002. DOI: 10.1021/la026082h. [Online]. Available: https://doi.org/10.1021/la026082h.

[26] K. H. Martin and P. A. Dayton, "Current status and prospects for microbubbles in ultrasound theranostics", *Wiley Interdisciplinary Reviews: Nanomedicine and Nanobiotechnology*, vol. 5, no. 4, pp. 329–345, Mar. 2013. DOI: 10.1002/wnan.1219. [Online]. Available: https://doi.org/10.1002/wnan.1219.

[27] *Journal of the Meteorological Society of Japan. Ser. II*, vol. 12, no. 5, pp. 265–266, 1934. DOI: 10.2151/jmsj1923.12.5_265. [Online]. Available: https://doi.org/10.2151/jmsj1923.12.5_265.

[28] D. W. Siemann, "The unique characteristics of tumor vasculature and preclinical evidence for its selective disruption by tumor-vascular disrupting agents", *Cancer Treatment Reviews*, vol. 37, no. 1, pp. 63–74, Feb. 2011. DOI: 10.1016/j.ctrv.2010.05.001. [Online]. Available: https://doi.org/10.1016/j.ctrv.2010.05.001.

[29] J. A. Nagy, S.-H. Chang, A. M. Dvorak, and H. F. Dvorak, "Why are tumour blood vessels abnormal and why is it important to know?", *British Journal of Cancer*, vol. 100, no. 6, pp. 865–869, Feb. 2009. DOI: 10.1038/sj.bjc.6604929. [Online]. Available: https://doi.org/10.1038/sj.bjc.6604929.

[30] S. Sindhwani, A. M. Syed, J. Ngai, B. R. Kingston, L. Maiorino, J. Rothschild, P. MacMillan, Y. Zhang, N. U. Rajesh, T. Hoang, J. L. Y. Wu, S. Wilhelm, A. Zilman, S. Gadde, A. Sulaiman, B. Ouyang, Z. Lin, L. Wang, M. Egeblad, and

W. C. W. Chan, "The entry of nanoparticles into solid tumours", *Nature Materials*, Jan. 2020. DOI: 10.1038/s41563-019-0566-2. [Online]. Available: https://doi.org/10.1038/s41563-019-0566-2.

[31] R. Suzuki, T. Takizawa, Y. Negishi, N. Utoguchi, and K. Maruyama, "Effective gene delivery with novel liposomal bubbles and ultrasonic destruction technology", *International Journal of Pharmaceutics*, vol. 354, no. 1-2, pp. 49–55, Apr. 2008. DOI: 10.1016/j.ijpharm.2007.10.034. [Online]. Available: https://doi.org/10.1016/j.ijpharm.2007.10.034.

[32] H. Wu, N. G. Rognin, T. M. Krupka, L. Solorio, H. Yoshiara, G. Guenette, C. Sanders, N. Kamiyama, and A. A. Exner, "Acoustic characterization and pharmacokinetic analyses of new nanobubble ultrasound contrast agents", *Ultrasound in Medicine & Biology*, vol. 39, no. 11, pp. 2137–2146, Nov. 2013. DOI: 10.1016/j.ultrasmedbio.2013.05.007. [Online]. Available: https://doi.org/10.1016/j.ultrasmedbio.2013.05.007.

[33] V. Paefgen, D. Doleschel, and F. Kiessling, "Evolution of contrast agents for ultrasound imaging and ultrasound-mediated drug delivery", *Frontiers in Pharmacology*, vol. 6, Sep. 2015. DOI: 10.3389/fphar.2015.00197. [Online]. Available: https://doi.org/10.3389/fphar.2015.00197.

[34] A. de Leon, R. Perera, C. Hernandez, M. Cooley, O. Jung, S. Jeganathan, E. Abenojar, G. Fishbein, A. J. Sojahrood, C. C. Emerson, P. L. Stewart, M. C. Kolios, and A. A. Exner, "Contrast enhanced ultrasound imaging by nature-inspired ultrastable echogenic nanobubbles", *Nanoscale*, vol. 11, no. 33, pp. 15 647–15 658, 2019. DOI: 10.1039/c9nr04828f. [Online]. Available: https://doi.org/10.1039/c9nr04828f.

[35] E. C. Unger, T. Porter, W. Culp, R. Labell, T. Matsunaga, and R. Zutshi, "Therapeutic applications of lipid-coated microbubbles", *Advanced Drug Delivery Reviews*, vol. 56, no. 9, pp. 1291–1314, May 2004. DOI: 10.1016/j.addr.2003.12.006. [Online]. Available: https://doi.org/10.1016/j.addr.2003.12.006.

[36] H. Haghi, A. J. Sojahrood, and M. C. Kolios, "On amplification of radial oscillations of microbubbles due to bubble-bubble interaction in polydisperse microbubble clusters under ultrasound excitation", *The Journal of the Acoustical Society of America*, vol. 143, no. 3, pp. 1862–1862, Mar. 2018. DOI: 10.1121/1.5036108. [Online]. Available: https://doi.org/10.1121/1.5036108.

[37] S. Manohar and D. Razansky, "Photoacoustics: A historical review", *Advances in Optics and Photonics*, vol. 8, no. 4, p. 586, Oct. 2016. DOI: 10.1364/aop.8.000586. [Online]. Available: https://doi.org/10.1364/aop.8.000586.

[38] J. Yao and L. V. Wang, "Sensitivity of photoacoustic microscopy", *Photoacoustics*, vol. 2, no. 2, pp. 87–101, Jun. 2014. DOI: 10.1016/j.pacs.2014.04.002. [Online]. Available: https://doi.org/10.1016%2Fj.pacs.2014.04.002.

[39] ——, "Photoacoustic tomography: Fundamentals, advances and prospects", *Contrast Media & Molecular Imaging*, vol. 6, no. 5, pp. 332–345, Sep. 2011. DOI:

10.1002/cmmi.443. [Online]. Available: https://doi.org/10.1002%2Fcmmi.443.

[40] *Biomedical Optics: Principles and Imaging*. Hoboken, N.J.: Wiley-Interscience, 2007.

[41] E. Bossy and S. Gigan, "Photoacoustics with coherent light", *Photoacoustics*, vol. 4, no. 1, pp. 22–35, Mar. 2016. DOI: 10.1016/j.pacs.2016.01.003. [Online]. Available: https://doi.org/10.1016/j.pacs.2016.01.003.

[42] P.-C. L. Emelianov Stanislav and M. O'Donnel, "Photoacoustics for molecular imaging and therapy", *Physics today*, vol. 62, no. 8, pp. 34–39, May 2009. [Online]. Available: https://www.ncbi.nlm.nih.gov/pmc/articles/PMC2879661/.

[43] C. Eker, "Optical characterization of tissue for medical diagnostics", PhD thesis, Lund Institute of Technology, Oct. 1999.

[44] S. L. Jacques, "Optical properties of biological tissues: A review", *Physics in Medicine and Biology*, vol. 58, no. 11, R37–R61, May 2013. DOI: 10.1088/0031-9155/58/11/r37. [Online]. Available: https://doi.org/10.1088%2F0031-9155%2F58%2F11%2Fr37.

[45] E. Petrova, A. Liopo, A. A. Oraevsky, and S. A. Ermilov, "Temperature-dependent optoacoustic response and transient through zero grüneisen parameter in optically contrasted media", *Photoacoustics*, vol. 7, pp. 36–46, Sep. 2017. DOI: 10.1016/j.pacs.2017.06.002. [Online]. Available: https://doi.org/10.1016/j.pacs.2017.06.002.

[46] Y.-H. Wang, A.-H. Liao, J.-H. Chen, C.-R. C. Wang, and P.-C. Li, "Photoacoustic/ultrasound dual-modality contrast agent and its application to thermotherapy", *Journal of Biomedical Optics*, vol. 17, no. 4, p. 045 001, 2012. DOI: 10.1117/1.jbo.17.4.045001. [Online]. Available: https://doi.org/10.1117/1.jbo.17.4.045001.

[47] G. Ku, K. Maslov, L. Li, and L. V. Wang, "Photoacoustic microscopy with 2-um transverse resolution", *Journal of Biomedical Optics*, vol. 15, no. 2, p. 021 302, 2010. DOI: 10.1117/1.3339912. [Online]. Available: https://doi.org/10.1117/1.3339912.

[48] K. Maslov, H. F. Zhang, S. Hu, and L. V. Wang, "Optical-resolution photoacoustic microscopy for in vivo imaging of single capillaries", *Optics Letters*, vol. 33, no. 9, p. 929, Apr. 2008. DOI: 10.1364/ol.33.000929. [Online]. Available: https://doi.org/10.1364/ol.33.000929.

[49] R. E. Borg and J. Rochford, "Molecular photoacoustic contrast agents: Design principles & applications", *Photochemistry and Photobiology*, vol. 94, no. 6, pp. 1175–1209, Aug. 2018. DOI: 10.1111/php.12967. [Online]. Available: https://doi.org/10.1111/php.12967.

[50] Q. Fu, R. Zhu, J. Song, H. Yang, and X. Chen, "Photoacoustic imaging: Contrast agents and their biomedical applications", *Advanced Materials*, p. 1 805 875, Dec. 2018. DOI: 10.1002/adma.201805875. [Online]. Available: https://doi.org/10.1002/adma.201805875.

[51] E. Petrova, S. Ermilov, R. Su, V. Nadvoretskiy, A. Conjusteau, and A. Oraevsky, "Using optoacoustic imaging for measuring the temperature dependence of grüneisen parameter in optically absorbing solutions", *Optics Express*, vol. 21, no. 21, p. 25 077, Oct. 2013. DOI: 10.1364/oe.21.025077. [Online]. Available: https://doi.org/10.1364/oe.21.025077.

[52] X. Zhang, S. Sun, T. Xu, and T. Zhang, "Temperature dependent grüneisen parameter", *Science China Technological Sciences*, vol. 62, no. 9, pp. 1565–1576, Aug. 2019. DOI: 10.1007/s11431-019-9526-3. [Online]. Available: https://doi.org/10.1007/s11431-019-9526-3.

[53] W. Li and X. Chen, "Gold nanoparticles for photoacoustic imaging", *Nanomedicine*, vol. 10, no. 2, pp. 299–320, Jan. 2015. DOI: 10.2217/nnm.14.169. [Online]. Available: https://doi.org/10.2217/nnm.14.169.

[54] S. Yoo, D. Jung, J.-J. Min, H. Kim, and C. Lee, "Biodegradable contrast agents for photoacoustic imaging", *Applied Sciences*, vol. 8, no. 9, p. 1567, Sep. 2018. DOI: 10.3390/app8091567. [Online]. Available: https://doi.org/10.3390/app8091567.

[55] A. D. L. Zerda, C. Zavaleta, S. Keren, S. Vaithilingam, S. Bodapati, Z. Liu, J. Levi, B. R. Smith, T.-J. Ma, O. Oralkan, Z. Cheng, X. Chen, H. Dai, B. T. Khuri-Yakub, and S. S. Gambhir, "Carbon nanotubes as photoacoustic molecular imaging agents in living mice", *Nature Nanotechnology*, vol. 3, no. 9, pp. 557–562, Aug. 2008. DOI: 10.1038/nnano.2008.231. [Online]. Available: https://doi.org/10.1038/nnano.2008.231.

[56] J. Weber, P. C. Beard, and S. E. Bohndiek, "Contrast agents for molecular photoacoustic imaging", *Nature Methods*, vol. 13, no. 8, pp. 639–650, Jul. 2016. DOI: 10.1038/nmeth.3929. [Online]. Available: https://doi.org/10.1038/nmeth.3929.

[57] G. P. Luke, D. Yeager, and S. Y. Emelianov, "Biomedical applications of photoacoustic imaging with exogenous contrast agents", *Annals of Biomedical Engineering*, vol. 40, no. 2, pp. 422–437, Nov. 2011. DOI: 10.1007/s10439-011-0449-4. [Online]. Available: https://doi.org/10.1007/s10439-011-0449-4.

[58] J. E. Lemaster and J. V. Jokerst, "What is new in nanoparticle-based photoacoustic imaging?", *Wiley Interdisciplinary Reviews: Nanomedicine and Nanobiotechnology*, vol. 9, no. 1, e1404, Apr. 2016. DOI: 10.1002/wnan.1404. [Online]. Available: https://doi.org/10.1002/wnan.1404.

[59] Ý. Mørch, R. Hansen, S. Berg, A. K. O. Åslund, W. R. Glomm, S. Eggen, R. Schmid, H. Johnsen, S. Kubowicz, S. Snipstad, E. Sulheim, S. Hak, G. Singh, B. H. McDonagh, H. Blom, C. de Lange Davies, and P. M. Stenstad, "Nanoparticle-stabilized microbubbles for multimodal imaging and drug delivery", *Contrast Media & Molecular Imaging*, vol. 10, no. 5, pp. 356–366, Apr. 2015. DOI: 10.1002/cmmi.1639. [Online]. Available: https://doi.org/10.1002/cmmi.1639.

[60] A. J. Dixon, S. Hu, A. L. Klibanov, and J. A. Hossack, "Oscillatory dynamics and in vivo photoacoustic imaging performance of plasmonic nanoparticle-coated microbubbles", *Small*, vol. 11, no. 25, pp. 3066–3077, Feb. 2015. DOI:

10.1002/smll.201403398. [Online]. Available: https://doi.org/10.1002/smll.201403398.

[61] A. Hannah, G. Luke, K. Wilson, K. Homan, and S. Emelianov, "Indocyanine green-loaded photoacoustic nanodroplets: Dual contrast nanoconstructs for enhanced photoacoustic and ultrasound imaging", *ACS Nano*, vol. 8, no. 1, pp. 250–259, Dec. 2013. DOI: 10.1021/nn403527r. [Online]. Available: https://doi.org/10.1021/nn403527r.

[62] E. Strohm, M. Rui, I. Gorelikov, N. Matsuura, and M. Kolios, "Vaporization of perfluorocarbon droplets using optical irradiation", *Biomedical Optics Express*, vol. 2, no. 6, p. 1432, May 2011. DOI: 10.1364/boe.2.001432. [Online]. Available: https://doi.org/10.1364/boe.2.001432.

[63] R. X. Xu, "Multifunctional microbubbles and nanobubbles for photoacoustic imaging", *Contrast Media & Molecular Imaging*, vol. 6, no. 5, pp. 401–411, Sep. 2011. DOI: 10.1002/cmmi.442. [Online]. Available: https://doi.org/10.1002/cmmi.442.

[64] Q. Chen, J. Yu, and K. Kim, "Review: Optically-triggered phase-transition droplets for photoacoustic imaging", *Biomedical Engineering Letters*, vol. 8, no. 2, pp. 223–229, May 2018. DOI: 10.1007/s13534-018-0069-0. [Online]. Available: https://doi.org/10.1007/s13534-018-0069-0.

[65] J. Yu, X. Chen, F. S. Villanueva, and K. Kim, "Vaporization and recondensation dynamics of indocyanine green-loaded perfluoropentane droplets irradiated by a short pulse laser", *Applied Physics Letters*, vol. 109, no. 24, p. 243 701, Dec. 2016. DOI: 10.1063/1.4972184. [Online]. Available: https://doi.org/10.1063/1.4972184.

[66] D. Y. Santiesteban, K. A. Hallam, S. K. Yarmoska, and S. Y. Emelianov, "Color-coded perfluorocarbon nanodroplets for multiplexed ultrasound and photoacoustic imaging", *Nano Research*, vol. 12, no. 4, pp. 741–747, Jan. 2019. DOI: 10.1007/s12274-019-2279-x. [Online]. Available: https://doi.org/10.1007/s12274-019-2279-x.

[67] G. Lajoinie, E. Gelderblom, C. Chlon, M. Böhmer, W. Steenbergen, N. de Jong, S. Manohar, and M. Versluis, "Ultrafast vapourization dynamics of laser-activated polymeric microcapsules", *Nature Communications*, vol. 5, no. 1, Apr. 2014. DOI: 10.1038/ncomms4671. [Online]. Available: https://doi.org/10.1038/ncomms4671.

[68] J. Jian, C. Liu, Y. Gong, L. Su, B. Zhang, Z. Wang, D. wang, Y. Zhou, F. Xu, P. Li, Y. Zheng, L. Song, and X. Zhou, "India ink incorporated multifunctional phase-transition nanodroplets for photoacoustic/ultrasound dual-modality imaging and photoacoustic effect based tumor therapy", *Theranostics*, vol. 4, no. 10, pp. 1026–1038, 2014. DOI: 10.7150/thno.9754. [Online]. Available: https://doi.org/10.7150/thno.9754.

[69] K. Wilson, K. Homan, and S. Emelianov, "Biomedical photoacoustics beyond thermal expansion using triggered nanodroplet vaporization for contrast-enhanced

imaging", *Nature Communications*, vol. 3, no. 1, Jan. 2012. DOI: 10.1038/ncomms1627. [Online]. Available: https://doi.org/10.1038/ncomms1627.

[70] W. Tang, Z. Yang, S. Wang, Z. Wang, J. Song, G. Yu, W. Fan, Y. Dai, J. Wang, L. Shan, G. Niu, Q. Fan, and X. Chen, "Organic semiconducting photoacoustic nanodroplets for laser-activatable ultrasound imaging and combinational cancer therapy", *ACS Nano*, vol. 12, no. 3, pp. 2610–2622, Feb. 2018. DOI: 10.1021/acsnano.7b08628. [Online]. Available: https://doi.org/10.1021/acsnano.7b08628.

[71] D. A. Fernandes and M. C. Kolios, "Perfluorocarbon bubbles as photoacoustic signal amplifiers for cancer theranostics", *Optical Materials Express*, vol. 9, no. 12, p. 4532, Nov. 2019. DOI: 10.1364/ome.9.004532. [Online]. Available: https://doi.org/10.1364/ome.9.004532.

[72] J. D. Dove, T. W. Murray, and M. A. Borden, "Enhanced photoacoustic response with plasmonic nanoparticle-templated microbubbles", *Soft Matter*, vol. 9, no. 32, p. 7743, 2013. DOI: 10.1039/c3sm51690c. [Online]. Available: https://doi.org/10.1039/c3sm51690c.

[73] Y. Toumia, F. Domenici, S. Orlanducci, F. Mura, D. Grishenkov, P. Trochet, S. Lacerenza, F. Bordi, and G. Paradossi, "Graphene meets microbubbles: A superior contrast agent for photoacoustic imaging", *ACS Applied Materials & Interfaces*, vol. 8, no. 25, pp. 16 465–16 475, Jun. 2016. DOI: 10.1021/acsami.6b04184. [Online]. Available: https://doi.org/10.1021/acsami.6b04184.

[74] D. Das, K. Sivasubramanian, C. Yang, and M. Pramanik, "On-chip generation of microbubbles in photoacoustic contrast agents for dual modal ultrasound/photoacoustic in vivo animal imaging", *Scientific Reports*, vol. 8, no. 1, Apr. 2018. DOI: 10.1038/s41598-018-24713-4. [Online]. Available: https://doi.org/10.1038/s41598-018-24713-4.

[75] M. Jeon, W. Song, E. Huynh, J. Kim, J. Kim, B. L. Helfield, B. Y. C. Leung, D. E. Goertz, G. Zheng, J. Oh, J. F. Lovell, and C. Kim, "Methylene blue microbubbles as a model dual-modality contrast agent for ultrasound and activatable photoacoustic imaging", *Journal of Biomedical Optics*, vol. 19, no. 1, p. 016 005, Jan. 2014. DOI: 10.1117/1.jbo.19.1.016005. [Online]. Available: https://doi.org/10.1117/1.jbo.19.1.016005.

[76] C. McEwan, C. Fowley, N. Nomikou, B. McCaughan, A. P. McHale, and J. F. Callan, "Polymeric microbubbles as delivery vehicles for sensitizers in sonodynamic therapy", *Langmuir*, vol. 30, no. 49, pp. 14 926–14 930, Dec. 2014. DOI: 10.1021/la503929c. [Online]. Available: https://doi.org/10.1021/la503929c.

[77] E. Huynh, J. F. Lovell, B. L. Helfield, M. Jeon, C. Kim, D. E. Goertz, B. C. Wilson, and G. Zheng, "Porphyrin shell microbubbles with intrinsic ultrasound and photoacoustic properties", *Journal of the American Chemical Society*, vol. 134, no. 40, pp. 16 464–16 467, Aug. 2012. DOI: 10.1021/ja305988f. [Online]. Available: https://doi.org/10.1021/ja305988f.

[78] N. Nomikou, C. Fowley, N. M. Byrne, B. McCaughan, A. P. McHale, and J. F. Callan, "Microbubble–sonosensitiser conjugates as therapeutics in sonodynamic therapy", *Chemical Communications*, vol. 48, no. 67, p. 8332, 2012. DOI: 10.1039/c2cc33913g. [Online]. Available: https://doi.org/10.1039/c2cc33913g.

[79] Y. Li, W. Huang, C. Li, and X. Huang, "Indocyanine green conjugated lipid microbubbles as an ultrasound-responsive drug delivery system for dual-imaging guided tumor-targeted therapy", *RSC Advances*, vol. 8, no. 58, pp. 33 198–33 207, 2018. DOI: 10.1039/c8ra03193b. [Online]. Available: https://doi.org/10.1039/c8ra03193b.

[80] F. J. Bodera, M. J. Moore, Y. Wang, A. C. D. Leon, E. Abenojar, A. A. Exner, and M. C. Kolios, "Nanobubble facilitated optoporation and photoacoustic imaging of bt-474 breast cancer cells", in *2018 IEEE International Ultrasonics Symposium (IUS) Ultrasonics Symposium (IUS), 2018 IEEE International*, IEEE, Oct. 2019.

[81] C. Ungureanu, R. Kroes, W. Petersen, T. A. M. Groothuis, F. Ungureanu, H. Janssen, F. W. B. van Leeuwen, R. P. H. Kooyman, S. Manohar, and T. G. van Leeuwen, "Light interactions with gold nanorods and cells: Implications for photothermal nanotherapeutics", *Nano Letters*, vol. 11, no. 5, pp. 1887–1894, May 2011. DOI: 10.1021/nl103884b. [Online]. Available: https://doi.org/10.1021/nl103884b.

[82] J. F. Lovell, C. S. Jin, E. Huynh, H. Jin, C. Kim, J. L. Rubinstein, W. C. W. Chan, W. Cao, L. V. Wang, and G. Zheng, "Porphysome nanovesicles generated by porphyrin bilayers for use as multimodal biophotonic contrast agents", *Nature Materials*, vol. 10, no. 4, pp. 324–332, Mar. 2011. DOI: 10.1038/nmat2986. [Online]. Available: https://doi.org/10.1038/nmat2986.

[83] E. Georgakopoulou, K Tsimaratou, K Evangelou, M.-P. Fernandez, V Zoumpourlis, I. Trougakos, D Kletsas, J Bartek, M Serrano, and V. Gorgoulis, "Specific lipofuscin staining as a novel biomarker to detect replicative and stress-induced senescence. a method applicable in cryo-preserved and archival tissues", *Aging*, vol. 5, no. 1, pp. 37–50, Dec. 2012. DOI: 10.18632/aging.100527. [Online]. Available: https://doi.org/10.18632/aging.100527.

[84] V. Gnyawali, J.-Z. Wang, Y. Wang, G. Fishbein, L. H. Y. So, A. C. D. Leon, E. Abenojar, A. A. Exner, S. S. H. Tsai, and M. C. Kolios, "Individual nanobubbles detection using acoustic based flow cytometry", in *Photons Plus Ultrasound: Imaging and Sensing 2019*, A. A. Oraevsky and L. V. Wang, Eds., SPIE, Feb. 2019. DOI: 10.1117/12.2510783. [Online]. Available: https://doi.org/10.1117/12.2510783.

[85] J. Owen and E. Stride, "Technique for the characterization of phospholipid microbubbles coatings by transmission electron microscopy", *Ultrasound in Medicine & Biology*, vol. 41, no. 12, pp. 3253–3258, Dec. 2015. DOI: 10.1016/j.ultrasmedbio.2015.07.024. [Online]. Available: https://doi.org/10.1016/j.ultrasmedbio.2015.07.024.

[86] C. Hernandez, E. C. Abenojar, J. Hadley, A. C. de Leon, R. Coyne, R. Perera, R. Gopalakrishnan, J. P. Basilion, M. C. Kolios, and A. A. Exner, "Sink or float? characterization of shell-stabilized bulk nanobubbles using a resonant mass measurement technique", *Nanoscale*, vol. 11, no. 3, pp. 851–855, 2019. DOI: 10.1039/c8nr08763f. [Online]. Available: https://doi.org/10.1039/c8nr08763f.

[87] A. F. Ph.D, *Subvisible particle characterization: Why simply counting shadows leaves you in the dark*, https://downstreamcolumn.com/ downstream-bioprocessing/ subvisible-particle-characterization-simply-counting-shadows-leaves-dark/, Accessed: 2020-06-03, May 2017.

[88] J. D. Berry, M. J. Neeson, R. R. Dagastine, D. Y. Chan, and R. F. Tabor, "Measurement of surface and interfacial tension using pendant drop tensiometry", *Journal of Colloid and Interface Science*, vol. 454, pp. 226–237, Sep. 2015. DOI: 10.1016/j.jcis.2015.05.012. [Online]. Available: https://doi.org/10.1016/j.jcis.2015.05.012.

[89] S. Iradji, "Optimization of subharmonic generation from ultrasound contrast agents at high frequency ultrasound", Master's thesis, Ryerson University, 2008.

[90] B. M. B. William Mendenhall Robert J. Beaver, *Introduction to Probability and Statistics*. Boston, MA.: Brooks Cole, Cengage Learning, 2013.

[91] C. Hernandez, L. Nieves, A. C. de Leon, R. Advincula, and A. A. Exner, "Role of surface tension in gas nanobubble stability under ultrasound", *ACS Applied Materials & Interfaces*, vol. 10, no. 12, pp. 9949–9956, Mar. 2018. DOI: 10.1021/acsami.7b19755. [Online]. Available: https://doi.org/10.1021/acsami.7b19755.

[92] P. S Epstein and M. S. Plesset, "On the stability of gas bubbles in liquid-gas solutions", *The Journal of chemical physics*, vol. 18, no. 11, pp. 1505–1509, Jan. 1950. DOI: 10.1063/1.1747520.

[93] P. B. Duncan and D. Needham, "Test of the epstein-plesset model for gas microparticle dissolution in aqueous media: Effect of surface tension and gas undersaturation in solution", *Langmuir*, vol. 20, no. 7, pp. 2567–2578, Mar. 2004. DOI: 10.1021/la034930i. [Online]. Available: https://doi.org/10.1021/la034930i.

[94] T. Leong, M. Ashokkumar, and S. Kentish, "The growth of bubbles in an acoustic field by rectified diffusion", in *Handbook of Ultrasonics and Sonochemistry*, Springer Singapore, 2015, pp. 1–30. DOI: 10.1007/978-981-287-470-2_74-1. [Online]. Available: https://doi.org/10.1007/978-981-287-470-2_74-1.

[95] H. Assadi, R. Karshafian, and A. Douplik, "Optical scattering properties of intralipid phantom in presence of encapsulated microbubbles", *International Journal of Photoenergy*, vol. 2014, pp. 1–9, 2014. DOI: 10.1155/2014/471764. [Online]. Available: https://doi.org/10.1155/2014/471764.

[96] P. Marmottant, S. van der Meer, M. Emmer, M. Versluis, N. de Jong, S. Hilgenfeldt, and D. Lohse, "A model for large amplitude oscillations of coated bubbles accounting for buckling and rupture", *The Journal of the Acoustical Society of America*, vol. 118, no. 6, pp. 3499–3505, Dec. 2005. DOI: 10.1121/1.2109427. [Online]. Available: https://doi.org/10.1121/1.2109427.

[97] J. Owen, C. McEwan, H. Nesbitt, P. Bovornchutichai, R. Averre, M. Borden, A. P. McHale, J. F. Callan, and E. Stride, "Reducing tumour hypoxia via oral administration of oxygen nanobubbles", *PLOS ONE*, vol. 11, no. 12, S. Rocha, Ed., e0168088, Dec. 2016. DOI: 10.1371/journal.pone.0168088. [Online]. Available: https://doi.org/10.1371/journal.pone.0168088.